Available online at www.sciencedirect.com
ScienceDirect
Journal of Computational Physics 227 (2008) 3849–3877
JOURNAL OF COMPUTATIONAL PHYSICS
www.elsevier.com/locate/jcp

A study of spectral element and discontinuous Galerkin methods for the Navier–Stokes equations in nonhydrostatic mesoscale atmospheric modeling: Equation sets and test cases ☆

F.X. Giraldo [a,*], M. Restelli [b]

[a] *Department of Applied Mathematics, Naval Postgraduate School, 833 Dyer Road, Monterey, CA 93943, USA*
[b] *MOX–Modellistica e Calcolo Scientifico, Dipartimento di Matematica, "F. Brioschi", Politecnico di Milano, via Bonardi 9 20133 Milano, Italy*

Received 8 May 2007; received in revised form 30 November 2007; accepted 3 December 2007
Available online 23 December 2007

Abstract

We present spectral element (SE) and discontinuous Galerkin (DG) solutions of the Euler and compressible Navier–Stokes (NS) equations for stratified fluid flow which are of importance in nonhydrostatic mesoscale atmospheric modeling. We study three different forms of the governing equations using seven test cases. Three test cases involve flow over mountains which require the implementation of non-reflecting boundary conditions, while one test requires viscous terms (density current). Including viscous stresses into finite difference, finite element, or spectral element models poses no additional challenges; however, including these terms to either finite volume or discontinuous Galerkin models requires the introduction of additional machinery because these methods were originally designed for first-order operators. We use the local discontinuous Galerkin method to overcome this obstacle. The seven test cases show that all of our models yield good results. The main conclusion is that equation set 1 (non-conservation form) does not perform as well as sets 2 and 3 (conservation forms). For the density current (viscous), the SE and DG models using set 3 (mass and total energy) give less dissipative results than the other equation sets; based on these results we recommend set 3 for the development of future multiscale research codes. In addition, the fact that set 3 conserves both mass and energy up to machine precision motives us to pursue this equation set for the development of future mesoscale models. For the bubble and mountain tests, the DG models performed better. Based on these results and due to its conservation properties we recommend the DG method. In the worst case scenario, the DG models are 50% slower than the non-conservative SE models. In the best case scenario, the DG models are just as efficient as the conservative SE models.
Published by Elsevier Inc.

Keywords: Compressible flow; Euler; Lagrange; Legendre; Navier–Stokes; Nonhydrostatic; Viscous flow

☆ This work relates to Department of the Navy Grant N00014-06-1-4023 issued by the Office of Naval Research Global. The United States Government has a royalty-free license throughout the world in all copyrightable material contained herein.
* Corresponding author. Tel.: +1 831 656 2293; fax: +1 831 656 2355.
E-mail address: fxgirald@nps.edu (F.X. Giraldo).

0021-9991/$ - see front matter Published by Elsevier Inc.
doi:10.1016/j.jcp.2007.12.009

1. Introduction

The recent paradigm shift in high-performance computing (HPC) is forcing many numerical weather prediction (NWP) operational centers to rethink the numerical methods that their models are based on. For example, the current trend in distributed-memory computing has moved toward clusters based on hundreds of thousands of cheap, commodity-based processors; the top three fastest computers in the world in 2007 have 212,000 (Lawrence Livermore National Laboratory, USA), 65,000 (Forschungszentrum Juelich, Germany), and 14,000 (New Mexico Computing Applications Center, USA). It is expected that clusters comprised of millions of processors will appear very soon. In order to take full advantage of computers with such high processor counts requires exploring numerical methods that are local in nature, have a large on-processor operation count, and a small communication footprint. Local high-order methods like the spectral element and discontinuous Galerkin methods have all of these properties and for this reason they have been successfully applied to a variety of problems.

Spectral element (SE) methods combine the local domain decomposition property of finite element (FE) methods with the high-order accuracy and weak numerical dispersion of spectral methods. SE methods have shown promise in many areas of the geosciences including: seismic wave propagation [33], deep Earth flows [13], climate [53,14], ocean [28,38], and numerical weather prediction [21,22]. These methods are high-order FE methods where the interpolation and integration points are chosen to be the Legendre–Gauss–Lobatto points.

In contrast, discontinuous Galerkin (DG) methods combine the local domain decomposition property of FE methods, the high-order accuracy and weak numerical dispersion of spectral methods, and the conservation properties of finite volume (FV) methods; in essence, DG methods are the high-order generalization of FV methods. There are two distinct types of DG methods: nodal (see [20,23]) and modal (see [12,59]), but in the current study we only consider the nodal approach introduced in [20] which uses the same machinery developed for SE methods such as quadrilateral grids, tensor product basis functions, and Legendre–Gauss–Lobatto grid points. It has been only very recent (since 2000) that the DG method first appeared in geophysical fluid dynamics (GFD) applications. However, implementations of the DG method in GFD have remained primarily restricted to shallow water flow (see [44,35,2,20,10,12,37,40,34,23,24]). To date, there has been no published work on either SE or DG methods for nonhydrostatic mesoscale atmospheric applications.

However, doing something for the first time is not a sufficient reason for developing a new model – the new model must have attractive properties not offered by existing models. The high-order accuracy, geometric flexibility to use any grid, and the scalability of SE and DG methods on large processor count computers are sufficient reasons for exploring this new class of models.

Almost all nonhydrostatic mesoscale models currently in existence are based on the finite difference (FD) method; examples include the following list of models: [4,5,11,17,25,26,29–32,39,42,43,46,48,57,58], and [60]. Included in this list are models such as ARPS (University of Oklahoma), COAMPS (US Navy), LM (German Weather Service), MC2 (Environment Canada), MM5 (Penn State/NCAR), NMM (National Center for Environmental Prediction), and WRF (NCAR). The only models in the literature not based on the FD method are the FV models found in [7] and [1], and the SE and DG models presented in our paper. One of the biggest advantages that SE and DG methods have over the FD method is that no terrain following coordinates of the type presented in [16] need to be included in the governing equations. Of course, the orography has to be accounted for in some manner but element-based Galerkin (EBG) methods, such as FE, SE, FV, and DG, incorporate the orography via the definition of the grid. EBG methods do not require either orthogonal grids or grids with specific directions (such as the I and J indices in FD models); EBG models are inherently unstructured and, while requiring additional data structures for bookkeeping, completely liberate the method from the grid. This freedom from the grid has major repercussions in the implementation of these methods on distributed-memory computers in that no halo is required which translates into truly local algorithms that require very little communication across processors; instead, the communication stencil consists of the perimeter values of each processor (see [21]). The advantage that SE and DG methods have over the FD and FV methods is that high-order solutions (greater than fourth order) can be constructed quite naturally within the framework – such high-order properties are desirable because they reduce the dispersion errors associated with the discrete spatial operators [19]. In fact, the SE and DG formulations proposed in

this paper allow for arbitrarily high-order spatial operators to be constructed by an input parameter; all the results presented in Section 6 use either 8th or 10th order polynomials per element.

It should be mentioned that there are other numerical methods in the literature that have much to offer nonhydrostatic mesoscale atmospheric modeling. Most notably are the weighted essentially non-oscillatory (WENO) [15,27,45], spectral finite volume (SFV) [56], and spectral difference (SD) [36] methods. These methods possess many of the best features of the DG method (such as high-order accuracy, conservation, and the promise of monotonicity). The reason we have chosen SE and DG methods for our study is that they can be constructed to high-order on unstructured grids (either with quadrilateral or triangular elements). WENO, SFV, and SD methods do not offer the same level of geometric flexibility to use unstructured grids in combination with high-order accuracy. There are triangular WENO schemes but only for very specific stencils (see [27] for unstructured WENO methods up to fourth order); this is true also for the SD method although this method is still in its infancy and higher order stencils will undoubtedly be constructed in the future. The SFV method, unfortunately, requires the elements to be planar which is of little use in our future work. In this paper we only consider x–z models but for the three-dimensional model, we envision using curved triangular prisms in order to take advantage of unstructured grids in the horizontal (x–y) direction; this will be most easily achieved with either SE or DG methods.

The remainder of the paper is organized as follows. Section 2 describes the three forms of the Euler and Navier–Stokes equations that we study in this work. In Section 3 we discuss the seven test cases used to compare our numerical models. Section 4 describes the spectral element and discontinuous Galerkin formulation of the governing equations including the basis functions, numerical fluxes, and boundary conditions. In Section 5 we describe the explicit third order Runge–Kutta method we use to march the equations in time and the filters for maintaining stability. In Section 6 we present the results of the SE and DG models using all seven test cases. Finally, in Section 7 we summarize the key findings of this research and propose future directions.

2. Governing equations

In this paper we study three different forms of the equations that govern the dynamics of nonhydrostatic atmospheric processes. These three equation sets are the Euler equations that have been used for many years in computational fluid dynamics (CFD). One of the sets that we explore is the complete compressible Navier–Stokes equations with the physical viscosity defined by the Stokes hypothesis. It should be pointed out, however, that we use viscosity for the Navier–Stokes equations only for comparing with other previously published model results (see the density current test in Section 6); the main focus of this work is on the inviscid form of the equations (i.e. the Euler equations). Specifically, we study the following three equation sets:

1. (set 1) the non-conservative form using Exner pressure, momentum, and potential temperature,
2. (set 2) the conservative form using density, momentum, and potential temperature, and
3. (set 3) the conservative form using density, momentum, and total energy.

For the purposes of this study we restrict ourselves to two dimensions (x–z) and omit the Coriolis terms.

2.1. Equation set 1

Equation set 1, which has been used extensively in mesoscale modeling, reads

$$\begin{aligned}
&\frac{\partial \pi}{\partial t} + \boldsymbol{u}\cdot\nabla\pi + \frac{R}{c_v}\pi\nabla\cdot\boldsymbol{u} = 0,\\
&\frac{\partial \boldsymbol{u}}{\partial t} + \boldsymbol{u}\cdot\nabla\boldsymbol{u} + c_p\theta\nabla\pi = -g\boldsymbol{k} + \mu\nabla^2\boldsymbol{u},\\
&\frac{\partial \theta}{\partial t} + \boldsymbol{u}\cdot\nabla\theta = \mu\nabla^2\theta,
\end{aligned} \tag{1}$$

where the solution vector is $(\pi, \boldsymbol{u}^{\mathcal{T}}, \theta)^{\mathcal{T}}$, $\pi = \left(\frac{p}{P_0}\right)^{R/c_p}$ is the Exner pressure, $\boldsymbol{u} = (u, w)^{\mathcal{T}}$ is the velocity field, $\theta = \frac{T}{\pi}$ is the potential temperature, and $\mathcal{T}$ denotes the transpose operator. In these equations P is the pressure,

P_0 is the pressure at the surface ($P_0 = 1 \times 10^5$ Pa) and T is the temperature. Other variables and symbols requiring definition are the gradient operator $\boldsymbol{\nabla} = (\frac{\partial}{\partial x}, \frac{\partial}{\partial z})^{\mathcal{T}}$, the gravitational constant g, the gas constant $R = c_p - c_v$, the specific heats for constant pressure and volume, c_p and c_v, the dynamic viscosity μ, and the directional vector along the vertical (z) direction $\boldsymbol{k} = (0, 1)^{\mathcal{T}}$. The viscosity, μ, is zero for all tests except for the density current.

The advantage that set 1 has over the other two sets is that it is completely self-contained, that is, it can be solved with only four equations defining the four unknowns (five in three-dimensions). The only disadvantage is that a model based on these equations cannot conserve either mass or energy. Note that the mass equation is defined by a conservation-like law for the Exner pressure which cannot be formally conserved. Existing mesoscale models based on similar equations to set 1 include (but are not limited to) ARPS [60] (University of Oklahoma), COAMPS [26] (US Navy), LM [17] (German Weather Service), MM5 [25] (Penn State/NCAR), and NMM [29] (NCEP).

Introducing the following splitting of the Exner pressure and potential temperature $\pi(\boldsymbol{x}, t) = \bar{\pi}(z) + \pi'(\boldsymbol{x}, t)$ and $\theta(\boldsymbol{x}, t) = \bar{\theta}(z) + \theta'(\boldsymbol{x}, t)$ where the mean values are in hydrostatic balance:

$$c_p \bar{\theta} \frac{\mathrm{d}\bar{\pi}}{\mathrm{d}z} = -g \tag{2}$$

allows us to rewrite Eq. (1) as

$$\begin{aligned}
&\frac{\partial \pi'}{\partial t} + \boldsymbol{u} \cdot \boldsymbol{\nabla} \pi' + w \frac{\mathrm{d}\bar{\pi}}{\mathrm{d}z} + \frac{R}{c_v} (\pi' + \bar{\pi}) \boldsymbol{\nabla} \cdot \boldsymbol{u} = 0, \\
&\frac{\partial \boldsymbol{u}}{\partial t} + \boldsymbol{u} \cdot \boldsymbol{\nabla} \boldsymbol{u} + c_p \theta \boldsymbol{\nabla} \pi' = g \frac{\theta'}{\bar{\theta}} \boldsymbol{k} + \mu \nabla^2 \boldsymbol{u}, \\
&\frac{\partial \theta'}{\partial t} + \boldsymbol{u} \cdot \boldsymbol{\nabla} \theta' + w \frac{\mathrm{d}\bar{\theta}}{\mathrm{d}z} = \mu \nabla^2 \theta,
\end{aligned} \tag{3}$$

which has been expanded and simplified in order to enforce hydrostasis; Eq. (3) is the form used for all the test cases in Section 6.

2.2. Equation set 2

Equation set 2 is gaining popularity in the literature because it is not too dissimilar from set 1 and is in conservation form (for the inviscid case only). These equations are written as follows:

$$\begin{aligned}
&\frac{\partial \rho}{\partial t} + \boldsymbol{\nabla} \cdot (\rho \boldsymbol{u}) = 0, \\
&\frac{\partial \rho \boldsymbol{u}}{\partial t} + \boldsymbol{\nabla} \cdot (\rho \boldsymbol{u} \otimes \boldsymbol{u} + P \mathcal{I}_2) = -\rho g \boldsymbol{k} + \boldsymbol{\nabla} \cdot (\mu \rho \boldsymbol{\nabla} \boldsymbol{u}), \\
&\frac{\partial \rho \theta}{\partial t} + \boldsymbol{\nabla} \cdot (\rho \theta \boldsymbol{u}) = \boldsymbol{\nabla} \cdot (\mu \rho \boldsymbol{\nabla} \theta),
\end{aligned} \tag{4}$$

where the conserved variables are $(\rho, \rho \boldsymbol{u}^{\mathcal{T}}, \rho\theta)^{\mathcal{T}}$, ρ is the density, $\boldsymbol{u} = (u, w)^{\mathcal{T}}$ is the velocity field, and θ is the potential temperature which we have defined previously. The pressure P which appears in the momentum equation is obtained by the equation of state

$$P = P_0 \left(\frac{\rho R \theta}{P_0} \right)^{\frac{c_p}{c_v}} \tag{5}$$

and is required in order to close the system. Additional terms requiring definition are the tensor product $\otimes$ and the rank-2 identity matrix $\mathcal{I}_2$; this term essentially converts the pressure (which is a scalar) into a tensor.

The advantage that set 2 has over set 1 is that it is in conservation form, which when using methods that are formally conservative, allows the model to conserve all quantities. Note, however, that if the discretization method is not formally conservative, then this set should have little or no advantage over set 1. Existing mesoscale models based on this equation set includes WRF [48] and the model by Ahmad and Lindeman [1].

Upon splitting of the density and potential temperature as $\rho(\boldsymbol{x},t) = \bar{\rho}(z) + \rho'(\boldsymbol{x},t)$ and $\theta(\boldsymbol{x},t) = \bar{\theta}(z) + \theta'(\boldsymbol{x},t)$ where the mean values are in hydrostatic balance, Eq. (4) can be written as

$$\begin{aligned}
&\frac{\partial \rho'}{\partial t} + \nabla\cdot(\rho\boldsymbol{u}) = 0,\\
&\frac{\partial \rho\boldsymbol{u}}{\partial t} + \nabla\cdot(\rho\boldsymbol{u}\otimes\boldsymbol{u} + P'\mathcal{I}_2) = -\rho' g\boldsymbol{k} + \nabla\cdot(\mu\rho\nabla\boldsymbol{u}),\\
&\frac{\partial \rho\theta'}{\partial t} + \nabla\cdot(\rho\theta\boldsymbol{u}) = \nabla\cdot(\mu\rho\nabla\theta),
\end{aligned} \tag{6}$$

where $P' = P - \overline{P}$ and $\overline{P} = P(\bar{\rho},\bar{\theta})$; Eq. (6) is the form used for all the test cases in Section 6.

2.3. Equation set 3

Equation set 3 is the form used in computational fluid dynamics (CFD, e.g. [18]) and has not been used in atmospheric studies because the energy equation uses total energy rather than potential temperature which then requires an additional step to compute potential temperature in order to use existing (moist) sub-grid scale physical parameterizations. However, as we show in this paper, this equation set has some advantages that may be worth considering for the development of future mesoscale numerical weather prediction (NWP) models.

These equations are written as follows:

$$\begin{aligned}
&\frac{\partial \rho}{\partial t} + \nabla\cdot(\rho\boldsymbol{u}) = 0,\\
&\frac{\partial \rho\boldsymbol{u}}{\partial t} + \nabla\cdot(\rho\boldsymbol{u}\otimes\boldsymbol{u} + P\mathcal{I}_2) = -\rho g\boldsymbol{k} + \nabla\cdot\boldsymbol{F}^{\mathrm{visc}}_{\boldsymbol{u}},\\
&\frac{\partial \rho e}{\partial t} + \nabla\cdot[(\rho e + P)\boldsymbol{u}] = \nabla\cdot\boldsymbol{F}^{\mathrm{visc}}_{e},
\end{aligned} \tag{7}$$

where the conserved variables are $(\rho, \rho\boldsymbol{u}^{\mathcal{T}}, \rho e)^{\mathcal{T}}$, ρ is the density, $\boldsymbol{u} = (u,w)^{\mathcal{T}}$ is the velocity field, $e = c_v T + \frac{1}{2}\boldsymbol{u}\cdot\boldsymbol{u} + \varphi$ is the total energy, and $\varphi = gz$ is the geopotential height. The pressure P is obtained by the equation of state which, in terms of the solution variables, is written as

$$P = \frac{R}{c_v}\rho\left(e - \frac{1}{2}\boldsymbol{u}\cdot\boldsymbol{u} - \varphi\right). \tag{8}$$

Note that the pressure, Eq. (8), for set 3 is less expensive to compute than the pressure for set 2 (Eq. (5)). This will be shown to have repercussions in the relative computational costs of these two equation sets.

The viscous fluxes $\boldsymbol{F}^{\mathrm{visc}}$ are defined as follows:

$$\boldsymbol{F}^{\mathrm{visc}}_{\boldsymbol{u}} = \mu[\nabla\boldsymbol{u} + (\nabla\boldsymbol{u})^{\mathcal{T}} + \lambda(\nabla\cdot\boldsymbol{u})\mathcal{I}_2] \tag{9}$$

and

$$\boldsymbol{F}^{\mathrm{visc}}_{e} = \boldsymbol{u}\cdot\boldsymbol{F}^{\mathrm{visc}}_{\boldsymbol{u}} + \frac{\mu c_p}{Pr}\nabla T, \tag{10}$$

where $\gamma = \frac{c_p}{c_v}$ is the specific heat ratio, $\lambda = -\frac{2}{3}$ comes from the Stokes hypothesis, and Pr is the Prandtl number.

This equation set directly represents the fundamental principles of conservation of mass, momentum and energy, and is physically consistent both in the inviscid and in the viscous regimes. In particular, when viscosity is present, it naturally accounts for the dissipative conversion of potential and kinetic energy into internal energy. In addition, from a more computationally oriented viewpoint, it should be noted that, since this is the equation set traditionally employed in CFD, much of the machinery developed in this field can be recycled; examples include total variation diminishing (TVD) schemes, slope limiters, and approximate Riemann solvers (e.g. see [18,55]).

Introducing the following splitting of the density and total energy $\rho(\boldsymbol{x},t) = \bar{\rho}(z) + \rho'(\boldsymbol{x},t)$ and $e(\boldsymbol{x},t) = \bar{e}(z) + e'(\boldsymbol{x},t)$, where the mean values are in hydrostatic balance, allows us to rewrite Eq. (7) as

$$\begin{aligned}
&\frac{\partial \rho'}{\partial t} + \nabla \cdot (\rho \boldsymbol{u}) = 0, \\
&\frac{\partial \rho \boldsymbol{u}}{\partial t} + \nabla \cdot (\rho \boldsymbol{u} \otimes \boldsymbol{u} + P' \mathcal{I}_2) = -\rho' g \boldsymbol{k} + \nabla \cdot \boldsymbol{F}_{\boldsymbol{u}}^{\text{visc}}, \\
&\frac{\partial \rho e'}{\partial t} + \nabla \cdot [(\rho e + P)\boldsymbol{u}] = \nabla \cdot \boldsymbol{F}_e^{\text{visc}},
\end{aligned} \tag{11}$$

which is the form used in all the test cases in Section 6; note that we were not able to find a single mesoscale model in the literature which uses this equation set.

2.4. Viscous stresses

It should be mentioned that only equation set 3 has the true viscous stresses; we use *ad hoc* diffusion terms for sets 1 and 2 merely for convenience. The viscous terms of set 2 would be identical to those of set 3 for the momentum if

$$\nabla \cdot (\mu \rho \nabla \boldsymbol{u}) \rightarrow \nabla \cdot \boldsymbol{F}_{\boldsymbol{u}}^{\text{visc}},$$

where the arrow signifies that the term on the left should be replaced by the one on the right. For the potential temperature, after much algebra, one would arrive at

$$\nabla \cdot (\mu \rho \nabla \theta) \rightarrow -\frac{1}{c_p \pi} \left(\nabla \cdot \left(-\frac{\mu c_p}{Pr} \nabla T \right) + \boldsymbol{F}_{\boldsymbol{u}}^{\text{visc}} \cdot \nabla \boldsymbol{u} \right).$$

These viscous terms can then be used to compute the true stresses of set 1. Specifically, for set 1 we would get for momentum

$$\mu \nabla^2 \boldsymbol{u} \rightarrow \frac{1}{\rho} \nabla \cdot \boldsymbol{F}_{\boldsymbol{u}}^{\text{visc}}$$

and for potential temperature

$$\mu \nabla^2 \theta \rightarrow -\frac{1}{c_p \pi \rho} \left(\nabla \cdot \left(-\frac{\mu c_p}{Pr} \nabla T \right) + \boldsymbol{F}_{\boldsymbol{u}}^{\text{visc}} \cdot \nabla \boldsymbol{u} \right).$$

There are two reasons why we do not use these stresses: the first reason is that for the purposes of intercomparison of our models with other previously published models we adhere to the equations used in Straka et al. [51] which use viscous stresses similar to those that we define for sets 1 (Eq. (1)) and 2 (Eq. (4)). The second reason for not using these stresses (at least for set 2) is that the equations would no longer be in conservation form. Due to these issues alone we recommend set 3 to be used for all future nonhydrostatic atmospheric models. For the purposes of this study it is not so important to use the true viscous stresses for sets 1 and 2 since viscosity is only used for one test case. Since no previous work using set 3 was found, we use the true Navier–Stokes viscosity (Eqs. (9) and (10)). Due to this discrepancy in the viscous stresses between the three equation sets, we expect slight differences in the results; the question is how large will these differences be.

3. Definition of the test cases

We now describe the seven test cases used to validate the numerical models. The set of test cases that we use is based on a list first proposed by Skamarock et al. [47]; we have added two bubble tests to the set. None of the cases uses Coriolis and only the density current test requires viscosity.

For all cases, we shall define the initial conditions in terms of Exner pressure, π, and potential temperature, θ. However, for equation sets 2 and 3 we require density, ρ, and for set 3 total energy, e. Thus the conversion from π and θ to ρ and e is as follows:

$$\rho = \frac{P_0}{R\theta} \pi^{\frac{c_v}{R}}$$

and

$$e = c_v \theta \pi + \frac{1}{2}\boldsymbol{u}\cdot\boldsymbol{u} + gz.$$

To simplify the description of the initial conditions we shall write the Exner pressure and potential temperature in terms of a mean value plus a perturbation, that is $\pi(\boldsymbol{x},t) = \bar{\pi}(z) + \pi'(\boldsymbol{x},t)$ and $\theta(\boldsymbol{x},t) = \bar{\theta}(z) + \theta'(\boldsymbol{x},t)$ where the reference state is in hydrostatic balance.

3.1. Case 1: Inertia-gravity waves

The nonhydrostatic inertia-gravity wave test involves the evolution of a potential temperature perturbation in a channel with periodic boundary conditions on the left and right boundaries. The initial perturbation radiates to the left and right symmetrically, but because of the mean horizontal flow, does not remain centered about the initial position. The initial conditions we use are identical to those of Skamarock and Klemp [46]; we provide the test case definition below for completeness. The initial state of the atmosphere is taken to have a constant mean flow of $\bar{u} = 20$ m/s in a uniformly stratified atmosphere with a Brunt-Väisälä frequency of $\mathcal{N} = 0.01$/s. Using the definition of Brunt-Väisälä frequency

$$\mathcal{N}^2 = g\frac{\mathrm{d}}{\mathrm{d}z}(\ln\bar{\theta}) \tag{12}$$

yields

$$\bar{\theta} = \theta_0 \mathrm{e}^{\frac{\mathcal{N}^2}{g}z}, \tag{13}$$

where the constant of integration is $\theta_0 = 300$ K. The Exner pressure is obtained from the hydrostatic balance, Eq. (2), as

$$\bar{\pi} = 1 + \frac{g^2}{c_p\theta_0\mathcal{N}^2}\left(\mathrm{e}^{-\frac{\mathcal{N}^2}{g}z} - 1\right). \tag{14}$$

In addition, the potential temperature is perturbed by the amount

$$\theta' = \theta_c \frac{\sin\left(\frac{\pi_c z}{h_c}\right)}{1 + \left(\frac{x - x_c}{a_c}\right)^2},$$

where $\theta_c = 0.01$ °C, $h_c = 10,000$ m, $a_c = 5000$ m, $x_c = 100,000$ m, and $\pi_c = 3.14159265$ is the Archimedes' (trigonometric) constant.

The domain is defined as $(x,z) \in [0,300,000] \times [0,10,000]$ m with $t \in [0,3000]$ s. No-flux boundary conditions are used along the bottom and top boundaries while periodic boundary conditions are used along the lateral boundaries.

3.2. Case 2: Rising thermal bubble

The rising thermal bubble test shows the evolution of a warm bubble in a constant potential temperature environment. Because the bubble is warmer than the ambient air it rises while deforming as a consequence of the shearing motion caused by the velocity field gradients until it forms a mushroom cloud. The initial conditions we use are similar to those of Robert [42] with the air mass initially at rest and in hydrostatic balance. Setting $\bar{\theta} =$ constant in (2) immediately provides for the Exner pressure. To drive the motion of the air, the following potential temperature perturbation is then added:

$$\theta' = \begin{cases} 0 & \text{for } r > r_c, \\ \frac{\theta_c}{2}\left[1 + \cos\left(\frac{\pi_c r}{r_c}\right)\right] & \text{for } r \leqslant r_c, \end{cases}$$

where $\theta_c = 0.5$ °C, π_c is the trigonometric constant, $r = \sqrt{(x - x_c)^2 + (z - z_c)^2}$ with the following constants: $\bar{\theta} = 300$ K, $r_c = 250$ m, and $(x,z) \in [0,1000]^2$ m with $t \in [0,700]$ s and $(x_c, z_c) = (500, 350)$ m. The boundary conditions for all four boundaries are no-flux.

3.3. Case 3: Robert smooth bubble

Test case 3 is similar to the Robert smooth bubble presented in [42]; however, we use a cosine wave instead of the Gaussian used in [42]. The definition of this case is almost identical to the rising thermal bubble except that the domain is now defined as $(x,z) \in [0,1000] \times [0,1500]$ m with $t \in [0,800]$ s and $(x_c, z_c) = (500, 260)$ m. Recall that in case 2, the bubble is initially positioned at $y_c = 350$ whereas now we lower this position and let the bubble evolve for an additional 100 s (from 700 s in case 2 to 800 s in case 3). The longer integration requires us to move the top boundary in order to avoid having the bubble hit this boundary.

3.4. Case 4: Density current

The density current test was proposed in [51] and concerns the evolution of a cold bubble dropped in a neutrally stratified atmosphere. Because the bubble is cold, it sinks eventually hitting the ground. At this point, the bubble begins to shear as it travels along the ground forming Kelvin–Helmholtz rotors. As discussed in [51], viscosity is required in order to obtain a grid-converged solution. The initial conditions for this case are quite similar to those of the rising thermal bubble; however, the differences are in the domain size and the shape of the cold cosine bubble. The potential temperature perturbation is defined as

$$\theta' = \frac{\theta_c}{2}[1 + \cos(\pi_c r)],$$

where $\theta_c = -15\ ^\circ\mathrm{C}$

$$r = \sqrt{\left(\frac{x - x_c}{x_r}\right)^2 + \left(\frac{z - z_c}{z_r}\right)^2}$$

and $r_c = 1$. The domain is defined as $(x,z) \in [0,25,600] \times [0,6400]$ m with $t \in [0,900]$ s and the center of the bubble is originally positioned at $(x_c, z_c) = (0, 3000)$ m with the size of the bubble defined by the parameters $(x_r, z_r) = (4000, 2000)$ m. The boundary conditions for all four boundaries are no-flux and a dynamic viscosity of $\mu = 75\ \mathrm{m}^2/\mathrm{s}$ is used. Note that we have defined only half the domain in the horizontal as proposed in Straka et al. [51].

3.5. Case 5: Schär mountain

The Schär mountain test concerns the steady-state solution of hydrostatic flow over a five-peak mountain chain, with steady inflow and outflow boundary conditions. The initial conditions and mountain profile are given in Schaï et al. [43] which we now provide for completeness. The initial state of the atmosphere is taken to have a constant mean flow of $\bar{u} = 10$ m/s in a uniformly stratified atmosphere with a Brunt-Väisälä frequency of $\mathcal{N} = 0.01$/s. Using the definition of Brunt-Väisälä frequency, Eq. (12) yields the reference potential temperature given in Eq. (13), the Exner pressure given in Eq. (14) where the constant of integration is taken to be $\theta_0 = 280$ K. The domain is defined as $(x,z) \in [-25,000, 25,000] \times [0, 21,000]$ m with $t \in [0,10]$ h. The mountain is defined as

$$h(x) = h_c \mathrm{e}^{-\left(\frac{x}{a_c}\right)^2} \cos^2\left(\frac{\pi_c x}{\lambda_c}\right)$$

with the parameters $h_c = 250$ m, $\lambda_c = 4000$ m, and $a_c = 5000$ m. This profile is shown in Fig. 1 where the axes have been magnified as follows $(x,z) \in [-10,000, 10,000] \times [0,1000]$ m in order to show the five peaks of the mountain. No-flux boundary conditions are used along the bottom surface while non-reflecting boundary conditions are used along the top and lateral boundaries. Note that this test is in the hydrostatic range since $\frac{\mathcal{N} a_c}{\bar{u}} > 1$.

3.6. Case 6: Linear hydrostatic mountain

The linear hydrostatic mountain test involves the steady-state solution of linear hydrostatic flow over a single-peaked mountain with constant inflow and outflow boundary conditions. The initial conditions and

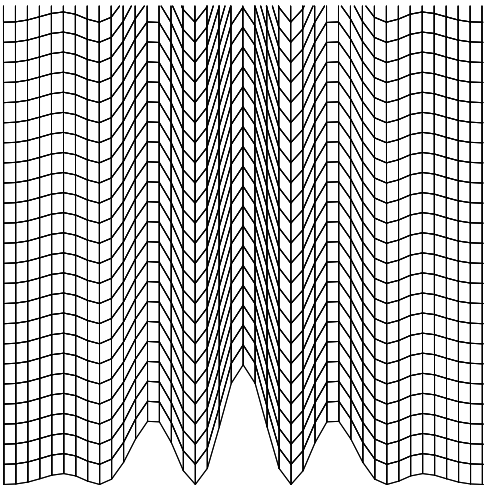

Fig. 1. Case 5: The Schär Mountain profile magnified such that $(x,z) \in [-10,000, 10,000] \times [0, 1000]$ m.

mountain profile are presented in Smith [49] and Durran and Klemp [11]. The initial state of the atmosphere consists of a constant mean flow with $\bar{u} = 20$ m/s in an isothermal atmosphere with constant temperature $\overline{T} = 250$ K. Since in the isothermal case we have $\mathcal{N} = \frac{g}{\sqrt{c_p \overline{T}}}$, the potential temperature and Exner pressure profiles are immediately provided by Eqs. (13) and (14), this latter reducing to

$$\bar{\pi} = e^{-\frac{g}{c_p \overline{T}} z}.$$

The domain is defined as follows: $(x,z) \in [0, 240, 000] \times [0, 30, 000]$ m with $t \in [0, 10]$ h with the *versiera di Agnesi* mountain profile defined as

$$h(x,z) = \frac{h_c}{1 + \left(\frac{x - x_c}{a_c}\right)^2}, \tag{15}$$

where $h_c = 1$ m, $x_c = 120,000$ m, and $a_c = 10,000$ m. It can be verified that $\frac{\mathcal{N} a_c}{\bar{u}} > 1$, so that the flow is in the hydrostatic range. Non-reflecting boundary conditions are required along the lateral and top boundaries. In addition, no-flux boundary conditions are used along the bottom.

3.7. Case 7: Linear nonhydrostatic mountain

The linear nonhydrostatic mountain test involves the steady-state solution of linear nonhydrostatic flow over a single-peaked mountain with constant inflow and outflow boundary conditions. For this test the initial state of the atmosphere consists of a constant mean flow of $\bar{u} = 10$ m/s in a uniformly stratified atmosphere with a Brunt-Väisälä frequency of $\mathcal{N} = 0.01$/s. Potential temperature and Exner pressure profiles are given by Eqs. (13) and (14), respectively, with $\theta_0 = 280$ K. The mountain profile given by Eq. (15) is used, with the numerical parameters now specified as $h_c = 1$ m, $x_c = 72,000$ m, and $a_c = 1000$ m. The computational domain is $(x,z) \in [0, 144, 000] \times [0, 30, 000]$ m with $t \in [0, 5]$ h. Note that since $\frac{\mathcal{N} a_c}{\bar{u}} = 1$ the flow is then in the nonhydrostatic regime. No-flux boundary conditions are used along the bottom and non-reflecting boundary conditions along the lateral and top boundaries.

4. Spatial discretization of the governing equations

For the sake of brevity, we shall only discuss the discretization of set 3 which we now write in the following compact vector form

$$\frac{\partial \boldsymbol{q}}{\partial t} + \nabla \cdot \boldsymbol{F} = S(\boldsymbol{q}), \tag{16}$$

where $\boldsymbol{q} = (\rho, \boldsymbol{U}^T, E)^T$ is the solution vector with $\boldsymbol{U} = \rho \boldsymbol{u}$ and $E = \rho e$, $\boldsymbol{F} = \boldsymbol{F}^{\text{inv}} - \boldsymbol{F}^{\text{visc}}$ is the total flux where

$$\boldsymbol{F}^{\text{inv}}(\boldsymbol{q}) = \begin{pmatrix} \boldsymbol{U} \\ \frac{\boldsymbol{U}\otimes\boldsymbol{U}}{\rho} + P\boldsymbol{\mathcal{I}}_2 \\ \frac{(E+P)\boldsymbol{U}}{\rho} \end{pmatrix} \tag{17}$$

is the inviscid flux tensor,

$$\boldsymbol{F}^{\text{visc}}(\boldsymbol{q}) = \mu \begin{pmatrix} 0 \\ \nabla \boldsymbol{u} + (\nabla \boldsymbol{u})^T + \lambda(\nabla \cdot \boldsymbol{u})\boldsymbol{\mathcal{I}}_2 \\ \boldsymbol{u} \cdot [\nabla \boldsymbol{u} + (\nabla \boldsymbol{u})^T + \lambda(\nabla \cdot \boldsymbol{u})\boldsymbol{\mathcal{I}}_2] + \frac{c_p}{Pr}\nabla T \end{pmatrix} \tag{18}$$

is the viscous flux tensor, and

$$S(\boldsymbol{q}) = -\begin{pmatrix} 0 \\ \rho g \boldsymbol{k} \\ 0 \end{pmatrix} \tag{19}$$

is the source function. Eq. (16) must be solved in $\Omega \times (0, T_{\text{final}})$, with $\Omega \subset \mathbb{R}^2$.

4.1. Basis functions, differentiation, and integration

To define the local operators which shall be used to construct the global approximation of the solution we begin by decomposing the domain Ω into N_e non-overlapping quadrilateral elements such that

$$\Omega = \bigcup_{e=1}^{N_e} \Omega_e.$$

We now define the reference element $\mathsf{I} = [-1, 1]^2$ and introduce for each element Ω_e the smooth, bijective transformation $\mathcal{F}_{\Omega_e}$ such that $\Omega_e = \mathcal{F}_{\Omega_e}(\mathsf{I})$. The notation $\boldsymbol{x} = \mathcal{F}_{\Omega_e}(\boldsymbol{\xi})$ will also be used, with $\boldsymbol{x} = (x, z) \in \Omega_e$ and $\boldsymbol{\xi} = (\xi, \eta) \in \mathsf{I}$. Associated with the map $\mathcal{F}_{\Omega_e}$ is the Jacobian $\boldsymbol{J}_{\Omega_e} = \frac{\mathrm{d}\mathcal{F}_{\Omega_e}}{\mathrm{d}\boldsymbol{\xi}}$, with determinant J_{Ω_e}. The Jacobian determinant of $\mathcal{F}_{\Omega_e}$ restricted to the boundary of I is denoted by $J^s_{\Omega_e}$. In both the SE and DG methods, an approximation $\boldsymbol{q}_N$ of the solution of Eq. (16) is sought such that, at each time level $t \in [0, T_{\text{final}}]$

$$\boldsymbol{q}_N(\cdot, t)|_{\Omega_e} = \psi \circ \mathcal{F}^{-1}_{\Omega_e}, \quad e = 1, \ldots, N_e,$$

where ψ is a function of the space $\mathcal{P}_N(\mathsf{I})$ of bivariate polynomials of degree lower than or equal to N in I

$$\mathcal{P}_N(\mathsf{I}) = \text{Span}\{\xi^n \eta^m | m, n \leqslant N, (\xi, \eta) \in \mathsf{I}\}, \quad N \geqslant 1.$$

A critical step is now the definition of a basis $\{\psi_k\}_{k=1}^K, K = (N+1)^2$, for $\mathcal{P}_N(\mathsf{I})$. The tensor product-structure of I allows us to construct such a basis as

$$\psi_{k_{ij}}(\boldsymbol{\xi}) = h_i(\xi) h_j(\eta),$$

where $\{h_i\}_{i=0}^N$ is a basis for $\mathcal{P}_N([-1, 1])$ and an index k_{ij} is biunivocally associated with the pair (i, j), with $i, j = 0, \ldots, N$. The basis functions $h_i(\xi)$ are in turn constructed as the Lagrangian polynomials associated with the Legendre–Gauss–Lobatto (LGL) points ξ_i given as the roots of

$$(1 - \xi^2) P'_N(\xi) = 0,$$

where $P_N(\xi)$ is the Nth order Legendre polynomial. Notice that associated with these points are the Gaussian quadrature weights

$$\omega_i = \frac{2}{N(N+1)} \left(\frac{1}{P_N(\xi_i)} \right)^2.$$

This fact will be exploited momentarily for the evaluation of local element integrals of $\boldsymbol{q}_N$.

With these definitions, we have

$$\boldsymbol{q}_N(\boldsymbol{x},t)|_{\Omega_e} = \sum_{k=1}^{K} \psi_k(\mathcal{F}_{\Omega_e}^{-1}(\boldsymbol{x}))\boldsymbol{q}_k(t), \quad e = 1,\ldots,N_e, \tag{20}$$

where we introduce the grid points $\boldsymbol{x}_{k_{ij}} = \mathcal{F}_{\Omega_e}((\xi_i,\eta_j))$ and the grid point values $\boldsymbol{q}_k(t) = \boldsymbol{q}_N(\boldsymbol{x}_k,t)$. The expansion given in Eq. (20) is essential in order to compute local element-wise derivatives and integrals. Concerning derivatives, in fact, it immediately provides

$$\left.\frac{\partial \boldsymbol{q}_N}{\partial \boldsymbol{x}}(\boldsymbol{x},t)\right|_{\Omega_e} = \sum_{k=1}^{K} \frac{\mathrm{d}}{\mathrm{d}\boldsymbol{x}}[\psi_k(\mathcal{F}_{\Omega_e}^{-1}(\boldsymbol{x}))]\boldsymbol{q}_k(t), \quad \left.\frac{\partial \boldsymbol{q}_N}{\partial t}(\boldsymbol{x},t)\right|_{\Omega_e} = \sum_{k=1}^{K} \psi_k(\mathcal{F}_{\Omega_e}^{-1}(\boldsymbol{x}))\frac{\mathrm{d}\boldsymbol{q}_k}{\mathrm{d}t}(t). \tag{21}$$

Concerning the computations of integrals, the expansion defined by Eq. (20) yields

$$\int_{\Omega_e} \boldsymbol{q}_N(\boldsymbol{x},t)\,\mathrm{d}\boldsymbol{x} = \int_{\mathrm{I}} \boldsymbol{q}_N(\boldsymbol{x}(\boldsymbol{\xi}),t)J_{\Omega_e}(\boldsymbol{\xi})\mathrm{d}\boldsymbol{\xi} \simeq \sum_{i,j=0}^{N} \omega_i\omega_j \boldsymbol{q}_{k_{ij}}(t)|J_{\Omega_e}(\xi_i,\eta_j)|. \tag{22}$$

4.2. Spectral element method

In the spectral element method, the following weak form approximation of Eq. (16) is considered: find $\boldsymbol{q}_N(\cdot,t) \in V_N^{\mathrm{SE}}$ such that

$$\int_{\Omega} \phi\left(\frac{\partial \boldsymbol{q}_N}{\partial t} + \boldsymbol{\nabla}\cdot\boldsymbol{F}(\boldsymbol{q}_N)\right)\mathrm{d}\Omega = \int_{\Omega} \phi S(\boldsymbol{q}_N)\mathrm{d}\Omega, \quad \forall\phi \in V_N^{\mathrm{SE}}, \tag{23}$$

where

$$V_N^{\mathrm{SE}} = \left\{\phi \in H^1(\Omega) : \phi|_{\Omega_e} = \psi \circ \mathcal{F}_{\Omega_e}^{-1}, \text{with } \psi \in \mathcal{P}_N(\mathrm{I}), e = 1,\ldots,N_e\right\}. \tag{24}$$

Notice that the two requirements $\phi \in H^1(\Omega)$ and $\phi|_{\Omega_e} = \psi \circ \mathcal{F}_{\Omega_e}^{-1}$ imply $V_N^{\mathrm{SE}} \subset C^0(\Omega)$. Integrating Eq. (23) by parts yields the equivalent problem: find $\boldsymbol{q}_N(\cdot,t) \in V_N^{\mathrm{SE}}$ such that

$$\int_{\Omega} \phi\frac{\partial \boldsymbol{q}_N}{\partial t}\,\mathrm{d}\Omega + \int_{\Gamma} \phi\boldsymbol{n}\cdot\boldsymbol{F}(\boldsymbol{q}_N)\mathrm{d}\Gamma - \int_{\Omega} \boldsymbol{\nabla}\phi\cdot\boldsymbol{F}(\boldsymbol{q}_N)\mathrm{d}\Omega = \int_{\Omega} \phi S(\boldsymbol{q}_N)\mathrm{d}\Omega, \quad \forall\phi \in V_N^{\mathrm{SE}}, \tag{25}$$

where $\boldsymbol{n}$ is the outward pointing normal vector on the domain boundary Γ. We point out that, although Eqs. (23) and (25) are in principle equivalent, they yield different numerical formulations when approximate quadrature formulas are adopted for the computation of the flux integrals, as is often the case. Such quadrature formulas in fact increase the computational efficiency of the scheme and diagonalize the mass matrix M to be defined shortly. In this paper, we shall use the form (25), since it allows for global conservation of mass, momentum, and energy even when approximating the integrals as in (22) [52].

By virtue of Eqs. (21) and (22), Eq. (25) yields the matrix problem

$$\frac{\mathrm{d}\boldsymbol{q}}{\mathrm{d}t} + (\widehat{\boldsymbol{M}}^s)^{\mathcal{T}}\boldsymbol{F}(\boldsymbol{q}) - \widehat{\boldsymbol{D}}^{\mathcal{T}}\boldsymbol{F}(\boldsymbol{q}) = S(\boldsymbol{q}), \tag{26}$$

where

$$\widehat{\boldsymbol{M}}^s = M^{-1}\boldsymbol{M}^s, \quad \widehat{\boldsymbol{D}} = M^{-1}\boldsymbol{D}$$

and $M, \boldsymbol{M}^s$ and $\boldsymbol{D}$ are the global mass, boundary and differentiation matrices, respectively. These latter are in turn constructed from their local counterparts $M^e, \boldsymbol{M}^{s,e}$ and $\boldsymbol{D}^e$ by means of the *direct stiffness summation* procedure

$$M = \bigwedge_{e=1}^{N_e} M^e, \quad \boldsymbol{M}^s = \bigwedge_{e=1}^{N_e} \boldsymbol{M}^{s,e}, \quad \boldsymbol{D} = \bigwedge_{e=1}^{N_e} \boldsymbol{D}^e,$$

where $\bigwedge_{e=1}^{N_e}$ denotes mapping the local degrees of freedom of each element Ω_e to the corresponding global degrees of freedom in Ω followed by summation (see [21] for further details). The local matrices are then defined as

$$M^e_{hk} = w_h |J_{\Omega_e}(\boldsymbol{\xi}_h)| \delta_{hk}, \quad \boldsymbol{D}^e_{hk} = w_h |J_{\Omega_e}(\boldsymbol{\xi}_h)| \nabla \phi_k(\boldsymbol{x}_h), \quad \boldsymbol{M}^{s,e}_{hk} = w^s_h |J^s_{\Omega_e}(\boldsymbol{\xi}_h)| \delta_{hk} \boldsymbol{n}(\boldsymbol{x}_h),$$

where $h,k = 1,\ldots,K$, δ_{hk} is the Kronecker delta, $\boldsymbol{\xi}_{k_{ij}} = (\xi_i, \eta_j), w_{k_{ij}} = \omega_i \omega_j, w^s_{k_{ij}} = \omega_i$ for $j = 0$ or $j = N$ and $w^s_{k_{ij}} = \omega_j$ for $i = 0$ or $i = N$.

4.3. Discontinuous Galerkin method

The discontinuous Galerkin method comes in various forms and flavors. For example, one could use either modal (amplitude–frequency space) or nodal (physical space) polynomial expansions. In this paper, we exploit the Lagrangian basis introduced in Section 4.1 to define a nodal DG formulation with inexact integration as proposed in [20]. Thus, the DG formulation that we describe below is essentially the discontinuous version of the SE formulation illustrated in Section 4.2. Alternatively, one could use exact integration (as in [23]) but as shown in [20] this would be more computationally expensive and thereby would not be competitive with the SE method.

In the DG method, Eq. (16) is multiplied by a test function ϕ and integrated over a generic element Ω_e, and the exact solution is replaced by its approximation, yielding

$$\int_{\Omega_e} \phi \left(\frac{\partial \boldsymbol{q}^e_N}{\partial t} + \nabla \cdot \boldsymbol{F}(\boldsymbol{q}^e_N) \right) \mathrm{d}\Omega = \int_{\Omega_e} \phi S(\boldsymbol{q}^e_N) \mathrm{d}\Omega_e, \tag{27}$$

where $\boldsymbol{q}^e_N$ denotes the degrees of freedom collocated in Ω_e. Applying now integration by parts and introducing the numerical flux $\boldsymbol{F}^*$, the following problem is obtained: find $\boldsymbol{q}_N(\cdot,t) \in V_N^{\mathrm{DG}}$ such that $\forall \Omega_e$, $e = 1,\ldots,N_e$

$$\int_{\Omega_e} \phi \frac{\partial \boldsymbol{q}^e_N}{\partial t} \mathrm{d}\Omega_e + \int_{\Gamma_e} \phi \boldsymbol{n} \cdot \boldsymbol{F}^*(\boldsymbol{q}_N) \mathrm{d}\Gamma_e - \int_{\Omega_e} \nabla \phi \cdot \boldsymbol{F}(\boldsymbol{q}^e_N) \mathrm{d}\Omega_e = \int_{\Omega_e} \phi S(\boldsymbol{q}^e_N) \mathrm{d}\Omega, \quad \forall \phi \in V_N^{\mathrm{DG}}, \tag{28}$$

where

$$V_N^{\mathrm{DG}} = \left\{ \phi \in L^2(\Omega) : \phi|_{\Omega_e} = \psi \circ \mathcal{F}^{-1}_{\Omega_e}, \text{with } \psi \in \mathcal{P}_N(\mathrm{I}), e = 1,\ldots,N_e \right\}. \tag{29}$$

Notice that, contrary to Eq. (24), there is no global continuity requirement, so that $V_N^{\mathrm{DG}} \not\in C^0(\Omega)$. This is possible because in Eq. (25) differentiability is required separately within each element, and not within the entire domain Ω. The coupling between neighboring elements is then recovered through the numerical flux $\boldsymbol{F}^*$, which is required to be a single valued function on the interelement boundaries and the precise definition of which is given below.

By virtue of Eqs. (21) and (22), Eq. (28) can be written in the matrix form

$$\frac{\mathrm{d}\boldsymbol{q}^e}{\mathrm{d}t} + (\widehat{\boldsymbol{M}}^{s,e})^{\mathcal{T}} \boldsymbol{F}^*(\boldsymbol{q}) - (\widehat{\boldsymbol{D}}^e)^{\mathcal{T}} \boldsymbol{F}(\boldsymbol{q}^e) = S(\boldsymbol{q}^e) \tag{30}$$

where $\widehat{\boldsymbol{M}}^{s,e} = (M^e)^{-1} \boldsymbol{M}^{s,e}$ and $\widehat{\boldsymbol{D}}^e = (M^e)^{-1} \boldsymbol{D}^e$. Note that this equation can be simplified to yield the following semi-discrete weak form:

$$\frac{\mathrm{d}\boldsymbol{q}^e_i}{\mathrm{d}t} = (\widehat{\boldsymbol{D}}^e_{ij})^{\mathcal{T}} \boldsymbol{F}^e_j + S^e_i - \frac{w^{s,e}_i |J^{s,e}_i|}{w^e_i |J^e_i|} (\boldsymbol{n}^{s,e}_i)^{\mathcal{T}} \boldsymbol{F}^*_i. \tag{31}$$

Further integration by parts in Eq. (28), and simplifying, yields the following semi-discrete strong DG formulation:

$$\frac{\mathrm{d}\boldsymbol{q}^e_i}{\mathrm{d}t} = -(\nabla \psi_{j,i})^{\mathcal{T}} \boldsymbol{F}^e_j + S^e_i + \frac{w^s_i |J^s_i|}{w^e_i |J^e_i|} \boldsymbol{n}^s_i (\boldsymbol{F}^e - \boldsymbol{F}^*)_i, \tag{32}$$

which looks very similar to a collocation penalty method in that no global matrix system needs to be constructed; it should be understood that this simple form is only possible by choosing the inexact integration DG form introduced in [20] which uses the same inexact integration theory and machinery used in the classical SE method.

4.3.1. Inviscid numerical flux

Substituting the boundary flux (Eq. (27)) with the numerical flux (Eq. (28)) is necessary in order to resolve the ambiguity in the definition of $\boldsymbol{q}_N$ on Γ_e (where it can attain two different values) and, by doing this, restoring the coupling between neighboring elements. Various choices are possible for the definition of $\boldsymbol{F}^*$; in the present study we use the Rusanov flux, mainly because of its simplicity but also because we have detected no discernible differences between the solution obtained with this flux function and the HLL, HLLC, or Roe's solver (see [18]). It is quite possible that for more stringent test cases (e.g. for shocks), differences between the various Riemann solvers may occur.

Upon arbitrarily associating to each interelement boundary an intrinsic tangential direction, so that a left (L) element and a right (R) element are identified, the Rusanov numerical flux can be expressed as

$$\boldsymbol{F}^{*,\text{inv}}(\boldsymbol{q}) = \frac{1}{2}[\boldsymbol{F}_N(\boldsymbol{q}_N^{\text{L}}) + \boldsymbol{F}_N(\boldsymbol{q}_N^{\text{R}}) - |\lambda|(\boldsymbol{q}_N^{\text{R}} - \boldsymbol{q}_N^{\text{L}})\boldsymbol{n}], \tag{33}$$

where $\lambda = \max(|U^{\text{L}}| + \sqrt{a^{\text{L}}}, |U^{\text{R}}| + \sqrt{a^{\text{R}}})$ with $U^{L,R} = \boldsymbol{u}^{L,R} \cdot \boldsymbol{n}$ being the normal component of velocity with respect to the edge Γ_e and $a = \sqrt{\gamma RT}$ being the speed of sound.

4.3.2. Viscous numerical flux

For the viscous form of the equations, the DG method is applied in a slightly different way. In fact, we use the *local discontinuous Galerkin* method first proposed in [3] and later analyzed in [8]. The idea is very similar to ideas put forth in the mixed finite element approach. In other words, rather than discretizing the Laplacian directly via a finite element approximation, we proceed in the following two-step approach. In Eqs. (9) and (10) we define the viscous fluxes for the Navier–Stokes equations as

$$\boldsymbol{\mathcal{U}} = \nabla \boldsymbol{u} \quad \text{and} \quad \boldsymbol{\mathcal{T}} = \nabla T.$$

Then, we apply the DG discretization in weak form and dividing through by the mass matrix obtaining

$$\boldsymbol{\mathcal{U}}_i^e = -(\widehat{\boldsymbol{D}}_{ij}^e)\boldsymbol{u}_j^e + \frac{w_i^{s,e}|J_i^{s,e}|}{w_i^e|J_i^e|}\boldsymbol{n}_i^{s,e}\boldsymbol{u}_i^* \quad \text{and} \quad \boldsymbol{\mathcal{T}}_i^e = -(\widehat{\boldsymbol{D}}_{ij}^e)T_j^e + \frac{w_i^{s,e}|J_i^{s,e}|}{w_i^e|J_i^e|}\boldsymbol{n}_i^{s,e}T_i^* \tag{34}$$

with $\boldsymbol{u}^* = \frac{1}{2}(\boldsymbol{u}^{\text{L}} + \boldsymbol{u}^{\text{R}})$ and $T^* = \frac{1}{2}(T^{\text{L}} + T^{\text{R}})$. Note that other choices are possible but we have chosen for simplicity the average value at the interface (see [8] for other choices). At this point, we can now discretize the viscous equations as

$$\frac{\mathrm{d}\boldsymbol{q}_i^e}{\mathrm{d}t} = (\widehat{\boldsymbol{D}}_{ij}^e)^{\mathcal{T}}\boldsymbol{F}_j^e + S(\boldsymbol{q}_i^e) - \frac{w_i^{s,e}|J_i^{s,e}|}{w_i^e|J_i^e|}\boldsymbol{n}_i^{s,e}\boldsymbol{F}_i^*, \tag{35}$$

where $\boldsymbol{F}^e = \boldsymbol{F}^{\text{inv}}(\boldsymbol{q}^e) - \boldsymbol{F}^{\text{visc}}(\boldsymbol{\mathcal{U}}^e, \boldsymbol{\mathcal{T}}^e)$, $\boldsymbol{F}^* = \boldsymbol{F}^{\text{inv}}(\boldsymbol{q}^*) - \boldsymbol{F}^{\text{visc}}(\boldsymbol{\mathcal{U}}^*, \boldsymbol{\mathcal{T}}^*)$, $\boldsymbol{\mathcal{U}}^* = \frac{1}{2}(\boldsymbol{\mathcal{U}}^{\text{L}} + \boldsymbol{\mathcal{U}}^{\text{R}})$, and $\boldsymbol{\mathcal{T}}^* = \frac{1}{2}(\boldsymbol{\mathcal{T}}^{\text{L}} + \boldsymbol{\mathcal{T}}^{\text{R}})$.

4.4. Boundary conditions

An important component of a mesoscale atmospheric model is the boundary conditions. For the test cases considered in this paper (and assuming a rectangular domain) the boundary conditions are: no-flux along the bottom boundary and either periodic, no-flux, or non-reflecting for the left and right boundaries, and either no-flux or non-reflecting for the top boundary.

4.4.1. Non-reflecting boundary conditions

Let us rewrite the governing equations as

$$\frac{\mathrm{d}\boldsymbol{q}}{\mathrm{d}t} = \cdots - \tau(\boldsymbol{q} - \bar{\boldsymbol{q}}),$$

where the ellipsis denotes the usual terms in the governing equations and the term τ is the coefficient of the absorbing sponge layer which relaxes the numerical solution to the prescribed reference value $\bar{\boldsymbol{q}}$. In terms of an explicit time-integrator, this becomes nothing more than

$$\boldsymbol{q}^{\text{sponged}} = \boldsymbol{q} - \tau(\boldsymbol{q} - \bar{\boldsymbol{q}}),$$

where $\boldsymbol{q}$ is the value obtained from the dynamical model, $\bar{\boldsymbol{q}}$ is the reference value, and $\boldsymbol{q}^{\text{sponged}}$ is the sponged variable; the parameter τ is a Lagrange multiplier that is found using a similar procedure to that presented in [11].

4.4.2. No-flux boundary conditions

The no-flux boundary conditions are enforced by virtue of the statement

$$\boldsymbol{n} \cdot \boldsymbol{u} = 0$$

at the boundaries. Thus, we seek to eliminate the normal component of the velocity to the no-flux boundary without altering the tangential component (we assume free slip boundary conditions for all test cases). The tangent vector to a boundary is obtained by $\boldsymbol{t} = \boldsymbol{k} \times \boldsymbol{n}$ which is equal to $\boldsymbol{t} = -n_z\boldsymbol{i} + n_x\boldsymbol{k}$. Thus we solve the following 2x2 system:

$$\begin{pmatrix} n_x & n_z \\ -n_z & n_x \end{pmatrix} \begin{pmatrix} u \\ w \end{pmatrix} = \begin{pmatrix} 0 \\ u_T \end{pmatrix},$$

where $u_T = \boldsymbol{t} \cdot \boldsymbol{u}$ is the tangential component of velocity.

For the inviscid equations (i.e. the Euler equations) the no-flux boundary condition on the momentum is all that is needed for all three equation sets. Concerning the viscous case, for equation sets 1 and 2, we simply impose a zero viscous flux for both momentum and temperature. For equation set 3, however, while imposing a zero viscous momentum flux is still appropriate, enforcing a zero viscous energy flux would result, in the case of a neutral atmosphere, in the development of a thermal boundary layer at the top and bottom boundaries. In this case in fact, since the viscous flux is controlled by the temperature gradient rather than by the potential temperature gradient, the viscous flux

$$\boldsymbol{F}_e^{\text{visc}} = \frac{\mu c_p}{Pr} \frac{\mathrm{d}\overline{T}}{\mathrm{d}z} \boldsymbol{k}$$

is required in order to maintain the neutral stratification. Hence, this latter flux, being required by the equations themselves and not by the numerical discretization, will be imposed in both the SE and DG formulations.

4.5. Numerical models

In Section 2 the following three equation sets were discussed: set 1 given by Eq. (3), set 2 given by Eq. (6), and set 3 given by Eq. (11). The eigenvalues of all three equation sets are $(U, U, U - \sqrt{a}, U + \sqrt{a})$ where $U = \boldsymbol{n} \cdot \boldsymbol{u}$ with $\boldsymbol{n}$ referring to a unit vector, and a is the speed of sound. It is important to know the eigenvalues in order to choose the maximum time-step which will allow the model to run in a stable fashion, and for constructing the numerical flux in the discontinuous Galerkin models.

In Section 4 the spectral element (SE) and discontinuous Galerkin (DG) methods were described. Based on the above three equation sets and the two numerical methods we have developed five numerical models which we compare in Section 6. Table 1 summarizes the five numerical models that we study.

Table 1 shows that there is no DG model for equation set 1; this is because equation set 1 is not in conservation form. Note that the momentum and energy equations can be written in conservation form as in equation set 2. However, to write the Exner pressure equation in conservation form requires adding (and

Table 1
Numerical models constructed in this study based on equation sets 1, 2, and 3 and the spectral element and discontinuous Galerkin methods

	Spectral element	Discontinuous Galerkin
Set 1 (Eq. (3))	SE1	–
Set 2 (Eq. (6))	SE2	DG2
Set 3 (Eq. (11))	SE3	DG3

subtracting) terms which will lead to a source term that cannot be avoided. If this is not troubling enough, the fluxes resulting from this system are non-physical and hence the DG method will not work. This then leaves us with only five numerical models.

5. Time-integrator and filters

In order to advance the solution in time while retaining some level of high-order accuracy, we use a strong stability preserving (SSP) Runge–Kutta third order (RK3) method of the type first proposed by Cockburn and Shu [9].

Definition 5.1. The solution $\boldsymbol{q}$ is said to be strongly stable if $\|\boldsymbol{q}^n\|_{\mathrm{TV}} \geqslant \|\boldsymbol{q}^{n+1}\|_{\mathrm{TV}} \forall\ n$.

Definition 5.2. The TV norm is defined as (see, e.g. [54]) $\|\boldsymbol{q}\|_{\mathrm{TV}} = \sum_{i=1}^{N_p-1} |\boldsymbol{q}_{i+1} - \boldsymbol{q}_i|$.

Let us write the semi-discrete (in space) equations as follows

$$\frac{\mathrm{d}\boldsymbol{q}}{\mathrm{d}t} = R(\boldsymbol{q}),$$

where $R(\boldsymbol{q})$ is the SE or DG representation of the term $S(\boldsymbol{q}) - \nabla \cdot \boldsymbol{F}(\boldsymbol{q})$ in Eq. (16) (where we assume a method of lines approach). The SSP temporal discretization of this vector equation is

$$\text{for } k = 1, \ldots, \mathrm{S} : \boldsymbol{q}^k = \alpha_0^k \boldsymbol{q}^n + \alpha_1^k \boldsymbol{q}^{k-1} + \beta^k \Delta t R(\boldsymbol{q}^{k-1}),$$

where $\boldsymbol{q}^0 = \boldsymbol{q}^n, \boldsymbol{q}^S = \boldsymbol{q}^{n+1}$, and S denotes the number of stages used. For all of our simulations we use the SSPRK (5, 3) method of Spiteri and Ruuth [50] which is a 5-stage third-order strong stability preserving Runge–Kutta method.

The time-step for all our simulations are chosen based on the maximum Courant number allowable by the time-integrator. For the purposes of this study we define the Courant number as

$$\text{Courant number} = \max \left(\frac{C\Delta t}{\Delta s} \right)_{HO}^{e} \forall e \in [1, \ldots, N_e],$$

where $C = |U + \sqrt{a}|$ is the characteristic speed, $U = \boldsymbol{n} \cdot \boldsymbol{u}$ is the velocity in the direction $\boldsymbol{n}$, a is the sound speed, and $\Delta s = \sqrt{\Delta x^2 + \Delta z^2}$ is the grid spacing. For all the results presented, the Courant number is taken to be 1.3 for the strong form SE method, Eq. (23), and 0.85 for the DG method (either strong or weak), and for the weak form SE method, Eq. (25); it turns out that imposing the boundary conditions weakly reduces the maximum allowable time-step. We shall report more on this in future work.

In order to maintain stability for long-time integrations, it is important not only to adhere to the CFL condition but also to control the Gibbs oscillations which affect all high-order methods in the absence of a dissipative mechanism (e.g. viscosity, slope limiters, etc.). The standard approach to avoid such instabilities is through the use of spatial filters of the Boyd–Vandeven type [6]. The filtering procedure is applied after each time-step as follows

$$\boldsymbol{q}_N^F = F \boldsymbol{q}_N,$$

where $\boldsymbol{q}_N^F$ denotes the filtered solution of the state variable $\boldsymbol{q}_N$, and F is the filter matrix defined in [21]; note that the filter matrix is very weak – in fact, only the highest modes are reduced by 5%.

6. Results

In this section we validate the five SE and DG numerical models on the test case suite of seven problems. For four of the seven problems that do not have analytic solutions we use symmetry and a comparison of extrema as metrics to discern the quality of the models.

For the three mountain problems we have semi-analytic solutions based on linear theory which require the application of a Fourier transform (see [49] for details). To obtain this semi-analytic solution we use a grid of 4000 (along x) by 100 (along z) points in order to ensure that the solution is exact within machine precision. In

addition, since the grid for the numerical and analytic solutions are different, we then interpolate both solutions to a grid of 400 (in x) by 100 (in z) defining a specific portion of the domain. This portion of the domain is the one that we use to plot and compute the root-mean-square (RMS) errors. We define the root-mean-square error as

$$\|\boldsymbol{q}\|_{\mathrm{RMS}} = \sqrt{\sum_{i=1}^{N_p} (\boldsymbol{q}^{\mathrm{numerical}} - \boldsymbol{q}^{\mathrm{analytic}})^2 / N_p},$$

where $N_p = 40,000$.

Following Smith [49], for the hydrostatic and nonhydrostatic mountains we define the momentum flux as

$$m(z) = \int_{-\infty}^{+\infty} \bar{\rho}(z) u(x,z) w(x,z) \mathrm{d}x,$$

where $\bar{\rho}(z)$ is the reference density as a function of height. From linear theory, the analytic hydrostatic momentum flux is given as

$$m^{\mathrm{H}}(z) = -\frac{\pi_c}{4} \bar{\rho}_s \bar{u}_s \mathcal{N} h_c^2, \tag{36}$$

where the superscript H signifies Hydrostatic, $\bar{\rho}_s$ and $\bar{u}_s$ are the reference density and horizontal velocity values at the surface, $\mathcal{N}$ is the Brunt-Väisälä frequency, and h_c is the height of the mountain.

Following Klemp and Durran [32], we define the analytic nonhydrostatic momentum flux as

$$m^{\mathrm{NH}}(z) = -0.457 m^{\mathrm{H}}(z),$$

where $m^{\mathrm{H}}(z)$ is given by Eq. (36). Note that, as pointed out by Klemp and Durran [32], this solution is valid only for $\frac{\mathcal{N} a_c}{\bar{u}} = 1$, which we specify *a priori*. The normalized momentum flux that we present below is then defined as either $m(z)/m^{\mathrm{H}}(z)$ or $m(z)/m^{\mathrm{NH}}(z)$, depending on whether the mountain problem is in the hydrostatic or nonhydrostatic regime.

6.1. Case 1: Inertia-gravity waves

Fig. 2a shows the potential temperature perturbation contours for DG3 after 3000 s and Fig. 2b shows the one-dimensional profile along $z = 5000$ m for all five models. Fig. 2b shows that all five models yield identical solutions – this is especially of interest since the models use different numerical methods and equation sets. The second observation is that the profiles are perfectly symmetric about the position $x = 160{,}000$ m. Note that

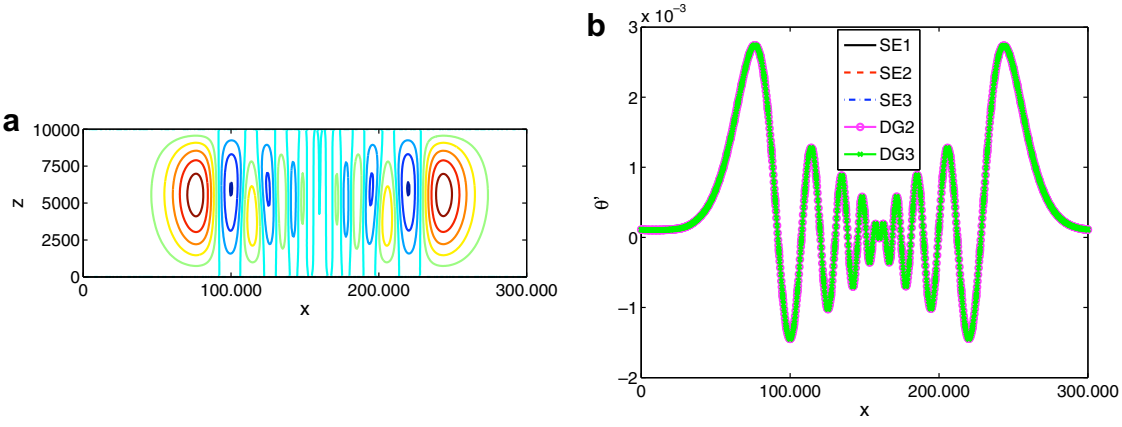

Fig. 2. Case 1: Inertia-gravity waves. Potential temperature perturbation after 3000 s for 250 m resolution and 10th-order polynomials. (a) shows the total domain using contour values between −0.0015 and 0.003 with a contour interval of 0.0005 and (b) shows the profiles along 5000 m height for all five models.

Table 2
Case 1: Inertia-gravity wave

Model	w_{max}	w_{min}	θ'_{max}	θ'_{min}
SE1	2.698×10^{-3}	-2.775×10^{-3}	2.787×10^{-3}	-1.518×10^{-3}
SE2	2.698×10^{-3}	-2.774×10^{-3}	2.787×10^{-3}	-1.519×10^{-3}
SE3	2.698×10^{-3}	-2.774×10^{-3}	2.787×10^{-3}	-1.519×10^{-3}
DG2	2.698×10^{-3}	-2.774×10^{-3}	2.787×10^{-3}	-1.519×10^{-3}
DG3	2.698×10^{-3}	-2.774×10^{-3}	2.787×10^{-3}	-1.519×10^{-3}

Comparison of the five models studied for 250 m resolution and 10th order polynomials after 3000 s.

there is a mean horizontal flow of 20 m/s which should move the initial perturbation from 100,000 m to 160,000 m in 3000 s; this is in fact what we get for all five models.

Skamarock and Klemp [46] give an analytic solution for this test but, unfortunately, it is only valid for the Boussinesq equations, which while useful for qualitative comparisons, cannot be used to compute error norms since we use the fully compressible equations. We use the same contouring interval used in [46] and our results look quite similar. In addition, we see that our results are very similar to those of the recently proposed FV model of Ahmad and Lindeman [1] which uses equation set 2. They use a smaller contouring interval but the potential temperature perturbations of our models have similar values. Specifically, their values are in the range $\theta' \in [-1.49 \times 10^{-3}, 2.82 \times 10^{-3}]$ whereas ours are $\theta' \in [-1.51 \times 10^{-3}, 2.78 \times 10^{-3}]$ which we show in Table 2.

Looking at Table 2 we note that our five models give exactly the same results except for SE1. We do not show the extrema for π' and u because they are identical for all five models; for π' they are $(-1.238 \times 10^{-6}, 1.716 \times 10^{-6})$ and for u they are $(-1.067 \times 10^{-2}, 1.069 \times 10^{-2})$. The differences in w_{min} and θ'_{min} for SE1 are certainly quite small but it is worth noting that SE1 is the only outlier. The results for this case can be summarized as follows: all five models yield very good results and sets 2 and 3 yield identical solutions, with set 1 being the only one that yields a different solution.

6.2. Case 2: Rising thermal bubble

Fig. 3 shows the potential temperature perturbation contours for DG3 after 700 s for various resolutions while Fig. 4 shows the one-dimensional profile along the vertical direction for $x = 500$ m. This case has no analytic solution but the resulting dynamics are sufficiently simple to be able to predict its proper evolution. Fig. 4a shows that at a 20 m resolution, when the bubble is under-resolved (see Fig. 3a) set 1 yields a different solution from sets 2 and 3. Note that all four models (SE2, SE3, DG2, and DG3) give the exact same results and SE1 being the only outlier. As we increase the resolution to 10 m (Fig. 4b) and to 5 m (Fig. 4c), the DG models (DG2 and DG3) yield a sharper discontinuity than the SE models (SE1, SE2, and SE3). The sharper discontinuity of the DG models can also be seen in Table 3 where the solution variables are tabulated for the 5 m resolution. The SE models yield almost identical results to each other while the DG models yield larger velocities yet smaller potential temperature extrema which result in a stronger and sharper discontinuity. Finally, at a 3.5 m resolution (Fig. 4d) all the models converge to the same solution.

The results for this test can be summarized as follows: set 1 should not be chosen for under-resolved flows; and the DG models are preferable to the SE models.

6.3. Case 3: Robert smooth bubble

Fig. 5 shows the potential temperature perturbation contours for DG3 after 700 and 800 s for a 5 m resolution while Fig. 6 shows the one-dimensional profile along the vertical direction for $x = 500$ m for all five models. Fig. 5 shows that from 700 to 800 s, the dynamics of the bubble changes from very smooth to turbulent. Fig. 6a shows that at 700 s, the SE solutions (SE1, SE2, and SE3) begin to separate from the DG solutions (DG2 and DG3). At this point, it is not known which solution is correct, but upon looking at Fig. 6b we see that at 800 s the SE solutions begin to oscillate wildly while the DG solutions maintain a sharp

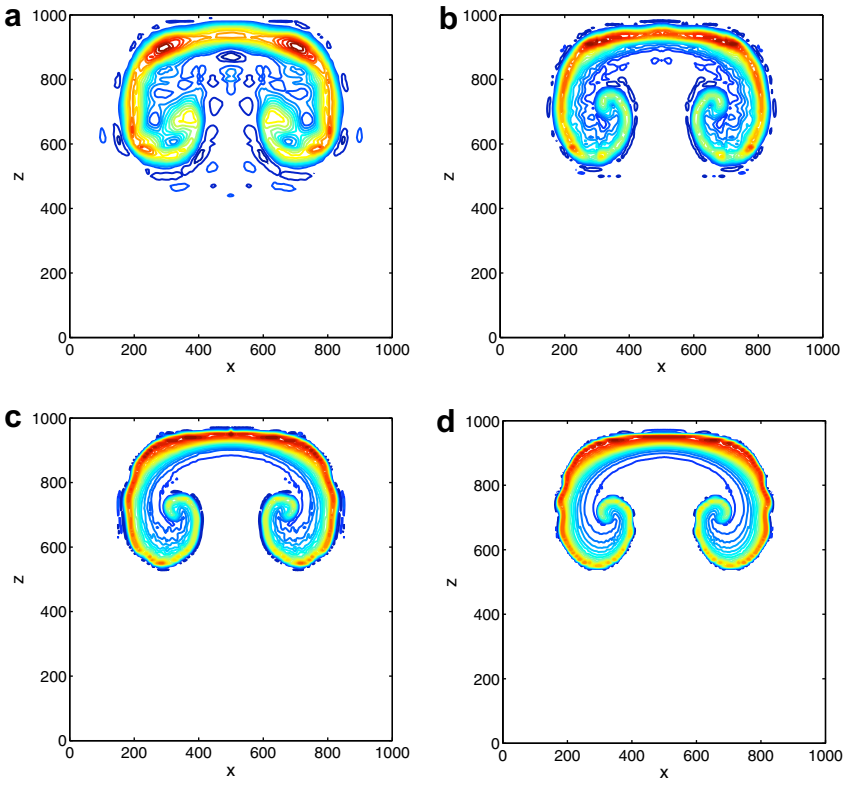

Fig. 3. Case 2: Rising Thermal Bubble. Potential temperature perturbation after 700 s for the following resolutions: (a) 20, (b) 10, (c) 5, and (d) 3.5 m. All resolutions use 10th order polynomials, and the contour values are from −0.05 to 0.525 with an interval of 0.025.

discontinuity. Table 4 confirms that the DG solutions indeed do a better job of capturing the discontinuity since it can be observed that the potential temperature (θ') extrema are smaller. The results for this test show that for strong gradients, the DG models are clearly preferable to the SE models. Note that we have not used any slope limiter or additional machinery with the DG method. Both the SE and DG models share the exact same machinery such as the spatial filters. This test highlights the advantages that the DG method may offer mesoscale modeling. In future work, we shall include slope limiters to the DG method in order to improve on the handling of discontinuities and other such sharp gradients.

6.4. Case 4: Density current

Fig. 7 shows the potential temperature perturbation contours after 900 s for 400, 200, 100, and 50 m resolutions. The first observation is that even at the very coarse resolution of 400 m (Fig. 7a), two of the three Kelvin–Helmholtz rotors are clearly visible. At a 200 m resolution (Fig. 7b) the second rotor is much better defined. At 100 m (Fig. 7c), all three rotors are clearly visible. Finally, at 50 m (Fig. 7d) there is little change in the structure of the rotors, the only discernible difference is that the noise above the rotors has disappeared.

In Fig. 8 we plot the one-dimensional profile of the potential temperature perturbation along the horizontal (x) direction at a height of $z = 1200$ m for all five models (on the left panel) and the profiles for five different resolutions (on the right panel). The three negative wells in Fig. 8a correspond to the three distinct rotors clearly visible in Fig. 7. Fig. 8a shows that the results for the five models split into two distinct groups. In one group, the three models SE1, SE2, and DG2 all give the same results and in the second group the models SE3 and DG3 give the same results. The differences between groups one and two are quite small but certainly not insignificant. This difference, however, is not unexpected since SE3 and DG3 use equation set 3 which has the true Navier–Stokes viscous stress. The main point that should be concluded from this figure is that the

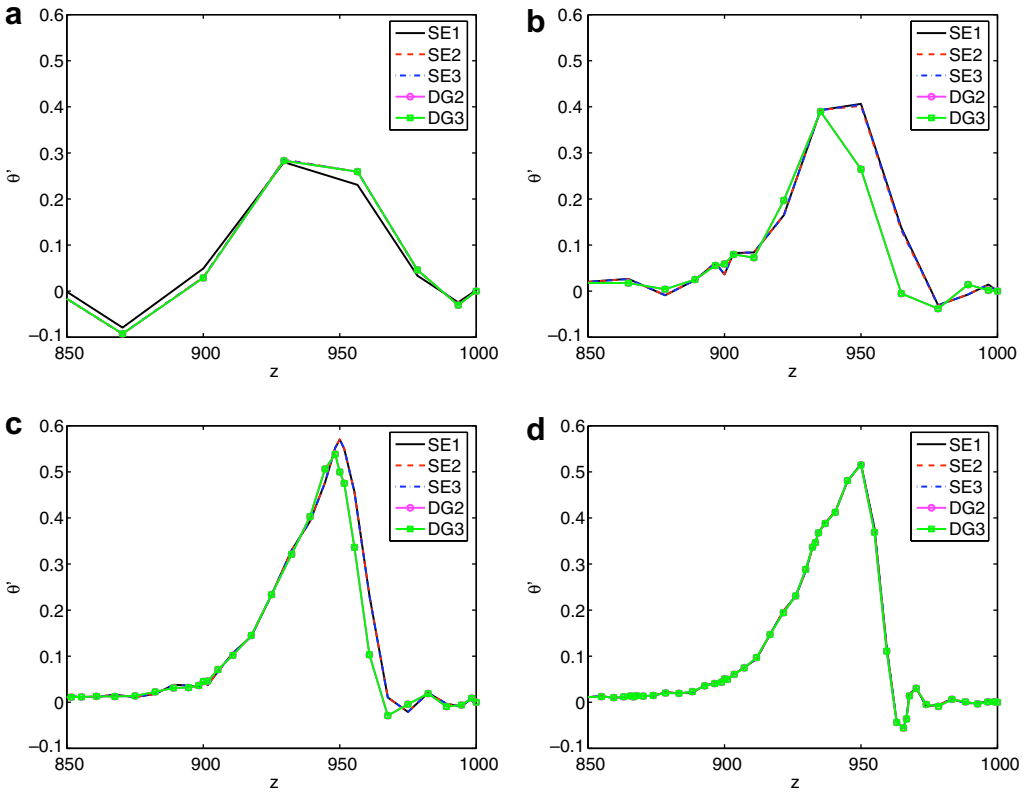

Fig. 4. Case 2: Rising Thermal Bubble. Potential temperature perturbation after 700 s for the following resolutions: (a) 20, (b) 10, (c) 5, and (d) 3.5 m. All resolutions use 10th order polynomials, and the profiles shown are along the vertical (z) at $x = 500$ m for all five models.

Table 3
Case 2: Rising thermal bubble

Model	π'_{max}	π'_{min}	u_{max}	u_{min}	w_{max}	w_{min}	θ'_{max}	θ'_{min}
SE1	9.364×10^{-6}	-1.195×10^{-5}	2.073	−2.073	2.536	−1.911	0.570	−0.098
SE2	9.364×10^{-6}	-1.196×10^{-5}	2.074	−2.074	2.536	−1.911	0.570	−0.098
SE3	9.365×10^{-6}	-1.196×10^{-5}	2.074	−2.074	2.536	−1.911	0.570	−0.098
DG2	9.355×10^{-6}	-1.195×10^{-5}	2.081	−2.081	2.543	−1.915	0.538	−0.093
DG3	9.355×10^{-6}	-1.195×10^{-5}	2.081	−2.081	2.543	−1.915	0.538	−0.093

Comparison of the five models studied for 5 m resolution and 10th order polynomials after 700 s.

equation set and not the numerical method has the larger impact on the solution for this test. To be convinced of this one only needs to look at Table 5 which we will discuss in a moment. Let us now turn to Fig. 8b to confirm that the models have indeed converged at 100 m resolution.

Fig. 8b shows that at 400 and 200 m resolutions, the potential temperature profiles are still changing. However, looking at either 100, 50, or 25 m resolutions one can see that all these curves are directly on top of each other; which confirms that our models have converged at 100 m resolution. Let us now turn to the results of Table 5.

Table 5 shows that the results for SE2 and DG2 are in fact identical and the results for SE3 and DG3 are also identical to each other; SE1 gives different results to SE2 and SE3, however, these differences are sufficiently small that they are unnoticeable in the one-dimensional profile plots.

In order to further quantify the differences between the five models, we use the same definition for the front location as in Straka et al. [51], that is, the −1 °C value of potential temperature perturbation. In Table 5 it is evident that all the models give essentially the same front location; for set 1 the front occurs earlier than for the

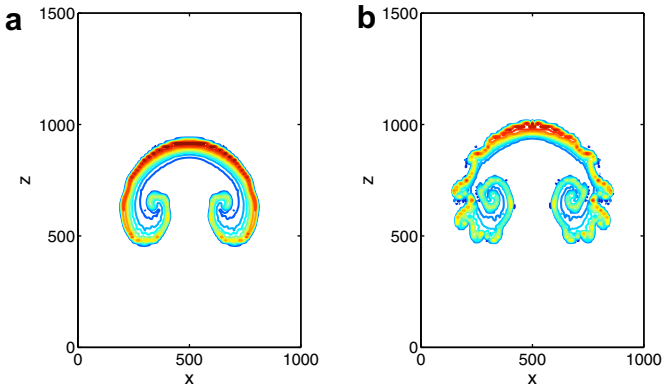

Fig. 5. Case 3: Robert Smooth Bubble. Potential temperature perturbation after (a) 700 and (b) 800 s. The contour values shown are from −0.1 to 0.6 with an interval of 0.05 using 10th order polynomials and a 5 m resolution.

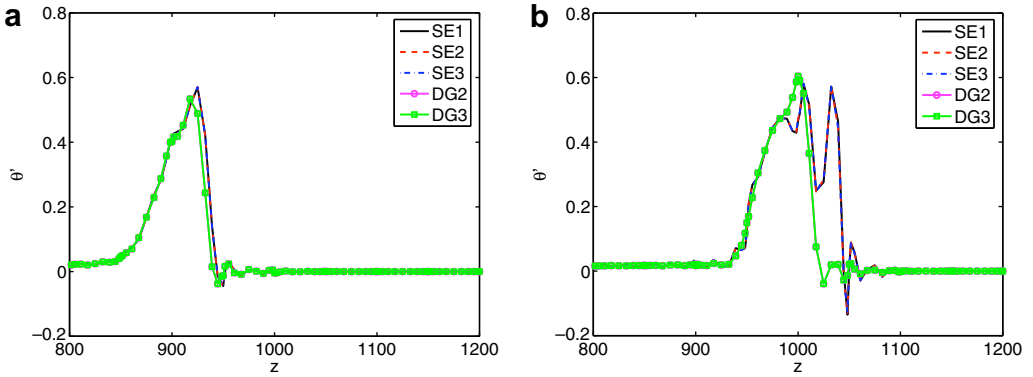

Fig. 6. Case 3: Robert Smooth Bubble. Potential temperature perturbation profiles after (a) 700 and (b) 800 s for all five models. The profiles shown are along the vertical (z) at $x = 500$ m using 10th order polynomials and a 5 m resolution.

Table 4
Case 3: Robert smooth bubble

Model	$\pi'_{\max}$	$\pi'_{\min}$	$u_{\max}$	$u_{\min}$	$w_{\max}$	$w_{\min}$	$\theta'_{\max}$	$\theta'_{\min}$
SE1	5.994×10^{-6}	-2.054×10^{-5}	2.471	−2.471	2.566	−2.510	0.625	−0.233
SE2	5.993×10^{-6}	-2.065×10^{-5}	2.493	−2.493	2.566	−2.529	0.624	−0.230
SE3	5.995×10^{-6}	-2.065×10^{-5}	2.493	−2.493	2.566	−2.529	0.624	−0.230
DG2	5.979×10^{-6}	-2.025×10^{-5}	2.423	−2.423	2.553	−2.335	0.604	−0.132
DG3	5.979×10^{-6}	-2.025×10^{-5}	2.423	−2.423	2.553	−2.335	0.604	−0.132

Comparison of the five models studied for 5 m resolution and 10th order polynomials after 800 s.

other two equation sets. Set 1 is more dissipative as indicated by the smaller potential temperature extrema. Equation set 2 gives less dissipative values for potential temperature and the front location thereby occurs later. Finally, equation set 3 yields the least dissipative solution and the front occurs even later for this set. The results for this case can be summarized as follows: set 3 is preferable to sets 1 and 2 – the choice of SE or DG is not as important as the equation set.

6.5. Case 5: Schär mountain

Fig. 9 shows that the numerical (solid) and analytic (dashed) values for both horizontal and vertical velocities compare quite well. In Table 6, we compare the RMS errors for all four variables for the five models.

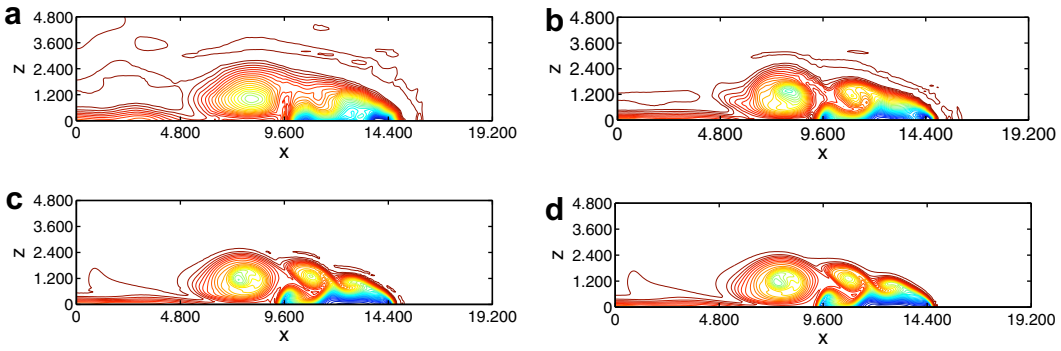

Fig. 7. Case 4: Density Current. Potential temperature perturbation after 900 s using (a) 400, (b) 200, (c) 100, and (d) 50 m resolution with 8th order polynomials. The contour values shown are between −9 to 0 with a contour interval of 0.25.

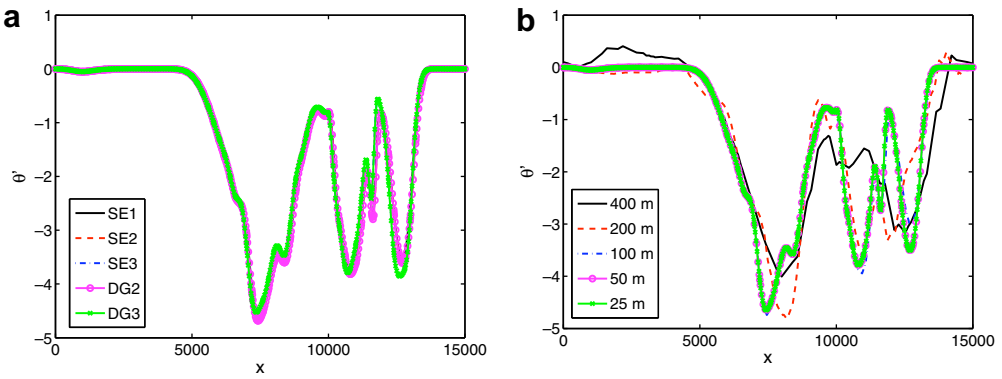

Fig. 8. Case 4: Density Current. Potential temperature perturbation after 900 s using 8th order polynomials for (a) all the models using 25 m resolution and (b) DG3 at five different resolutions (400 m, etc.). Profiles along 1200 m height are illustrated.

Table 5
Case 4: Density current

Model	Front location (in m)	π'_{max}	π'_{min}	θ'_{max}	θ'_{min}
SE1	14,736	8.431×10^{-4}	-1.662×10^{-2}	0.00059	−8.83
SE2	14,767	8.428×10^{-4}	-1.657×10^{-2}	0.00012	−8.90
SE3	14,789	8.361×10^{-4}	-1.690×10^{-2}	0.00331	−9.08
DG2	14,767	8.428×10^{-4}	-1.657×10^{-2}	0.00012	−8.90
DG3	14,789	8.361×10^{-4}	-1.690×10^{-2}	0.00331	−9.08

Comparison of the five models studied for 25 m resolution and 8th order polynomials after 900 s.

Clearly, all five models give essentially identical results; the differences between the models are quite small. Nonetheless, the results for SE1 are slightly better than those for SE2 and SE3. Looking at the rest of the models we see that DG2 and DG3 give better results than any of the SE models. For this test, the conclusion is that one should use DG over SE.

6.6. Case 6: Linear hydrostatic mountain

Fig. 10 shows that the numerical (solid) and analytic (dashed) values for both horizontal and vertical velocities compare quite well. Clearly, the vertical velocity is captured better than the horizontal velocity as can be seen in Table 7 where we see that the RMS errors differ by almost two orders of magnitude. This is not

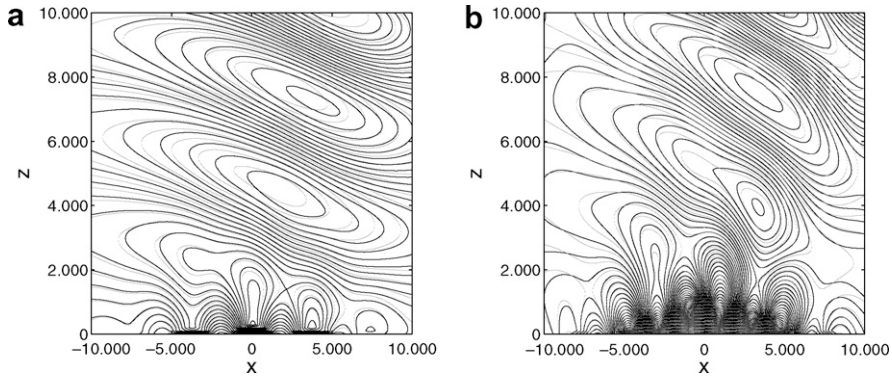

Fig. 9. Case 5: Schär Mountain. The numerical solution (solid line) and analytic solution (dashed line) after 10 h for 250 m (in x) and 210 m (in z) resolution and 10th order polynomials. For the horizontal velocity (a) the contour values are between -2 to $+2$ with a contour interval of 0.2. For the vertical velocity (b) the contour values are between -2 to $+2$ with a contour interval of 0.05.

Table 6
Case 5: Schär mountain

Variable	SE1	SE2	SE3	DG2	DG3
π	8.20×10^{-6}	8.29×10^{-6}	8.27×10^{-6}	7.37×10^{-6}	7.36×10^{-6}
u	2.26×10^{-1}	2.26×10^{-1}	2.26×10^{-1}	1.94×10^{-1}	1.94×10^{-1}
w	7.58×10^{-2}	7.67×10^{-2}	7.66×10^{-2}	7.51×10^{-2}	7.51×10^{-2}
θ	6.88×10^{-2}	6.80×10^{-2}	6.78×10^{-2}	5.85×10^{-2}	5.84×10^{-2}

Root-mean-square errors for all four variables after 10 h for 250 m (in x) and 210 m (in z) resolution and 10th order polynomials for all five models.

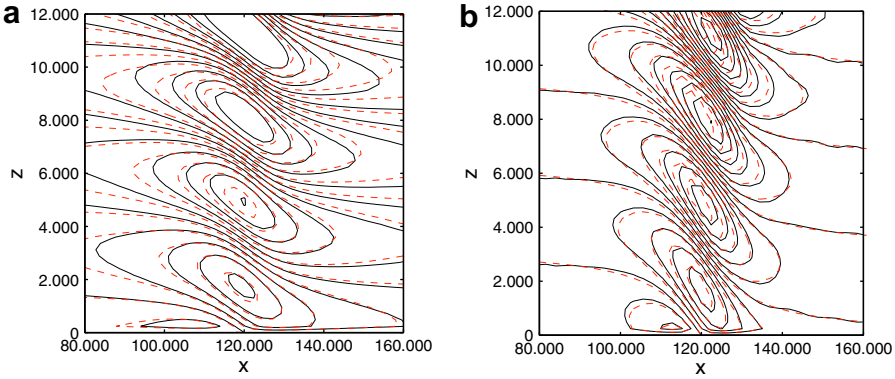

Fig. 10. Case 6: Linear Hydrostatic Mountain. The numerical solution (solid line) and analytic solution (dashed line) after 10 h for 1200 m (in x) and 240 m (in z) resolution and 10th order polynomials. For the horizontal velocity (a) the contour values are between -0.025 to $+0.025$ with a contour interval of 0.005. For the vertical velocity (b) the contour values are between -0.005 to $+0.005$ with a contour interval of 0.0005.

surprising for this case since it is in the hydrostatic regime and, thereby, the vertical acceleration does not play a dominant role.

There are a number of interesting observations that can be discerned from Table 7. The first is that all five models give relatively similar results. The second observation is that the DG models give slightly better results than the SE models; one can clearly see this by comparing the RMS errors for π', u, and w (except for θ'). The third observation is that equation sets 2 and 3 give better results than equation set 1. Note that SE1, SE2, and SE3 all use spectral elements – the only difference between these three models

Table 7
Case 6: Linear hydrostatic mountain

Variable	SE1	SE2	SE3	DG2	DG3
π	1.21×10^{-7}	1.21×10^{-7}	1.21×10^{-7}	1.20×10^{-7}	1.20×10^{-7}
u	2.28×10^{-3}	2.24×10^{-3}	2.24×10^{-3}	2.23×10^{-3}	2.23×10^{-3}
w	5.98×10^{-5}	4.31×10^{-5}	4.31×10^{-5}	3.20×10^{-5}	3.20×10^{-5}
θ	1.67×10^{-3}	1.64×10^{-3}	1.64×10^{-3}	1.65×10^{-3}	1.65×10^{-3}

Root-mean-square errors for all four variables for 1200 m (in x) and 240 m (in z) resolution and 10th order polynomials after 10 h for all five models.

is the equation sets used. Finally, the last observation is that equation sets 2 and 3 yield identical results when using the same numerical method.

In Fig. 11 we plot the normalized momentum flux for DG3 at various times in the integration (Fig. 11a) and for all five models after 10 h (Fig. 11b). Fig. 11a shows that the simulations have reached steady-state after 10 h. Fig. 11b shows that the normalized momentum flux values are almost identical for all five models and are quite good, that is, the values are between 0.95 and 1.01 – the best one could do is to have values of unity which we approach quite quickly. The results of this test case can be summarized as follows: all things being equal, one should use sets 2 or 3 instead of set 1 and DG is slightly better than SE.

6.7. Case 7: Linear nonhydrostatic mountain

Fig. 12 shows the horizontal and vertical velocity contours for DG3 after 5 h. Note how different the vertical velocity fields look between the nonhydrostatic (Fig. 12) and hydrostatic (Fig. 10) cases. In Fig. 12 we compare the numerical solution (solid lines) with the analytic solution (dashed lines). The simulated horizontal velocity (Fig. 12a) compares quite well with the analytic solution near the mountain but loses accuracy away from the mountain. In contrast, the simulated vertical velocity (Fig. 12b) compares extremely well with the analytic solution everywhere.

In Fig. 13 we plot the normalized momentum flux for DG3 at various times in the integration (Fig. 13a) and for all five models after 5 h (Fig. 13b). Fig. 13a shows that the simulations have reached steady-state after 5 h; this is clearly seen by the convergence of the momentum fluxes for times 3, 4, and 5 h. Fig. 13b shows that all five models give very similar momentum flux values. In fact, the values are very good since they remain between 0.95 and 1.

In Table 8 we list the RMS errors for all four variables of the five models. These results show that all five models, once again, yield very similar results. Although the differences in the RMS errors are quite small it can be seen that: SE2 and SE3 give better results than SE1; and DG2 and DG3 give better results than the SE

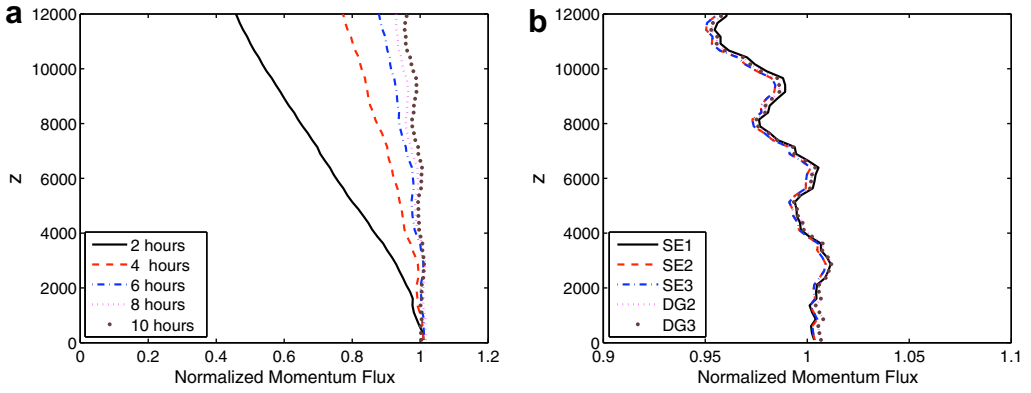

Fig. 11. Case 6: Linear Hydrostatic Mountain. Normalized momentum flux for 1200 m (in x) and 240 m (in z) resolution and 10th order polynomials for (a) DG3 at times 2, 4, 6, 8, and 10 h, and (b) for all five models at 10 h.

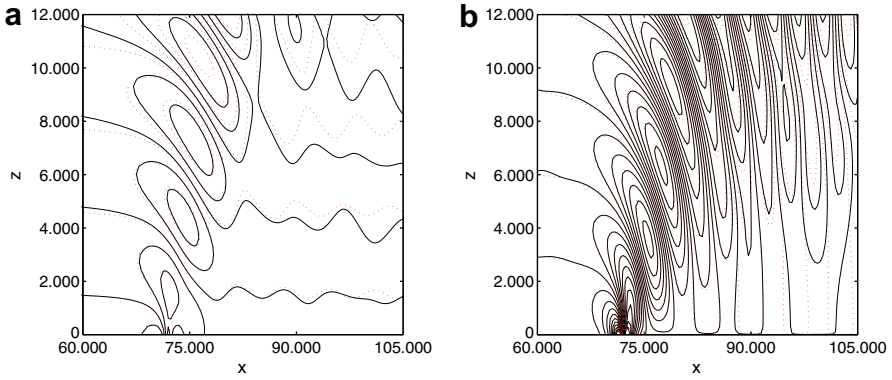

Fig. 12. Case 7: Linear Nonhydrostatic Mountain. The numerical solution (solid line) and analytic solution (dashed line) after 5 h for 360 m (in x) and 300 m (in z) resolution and 10th order polynomials. For the horizontal velocity (a) the contour values are between -0.025 to $+0.025$ with a contour interval of 0.0025. For the vertical velocity (b) the contour values are between -0.005 to $+0.005$ with a contour interval of 0.0005.

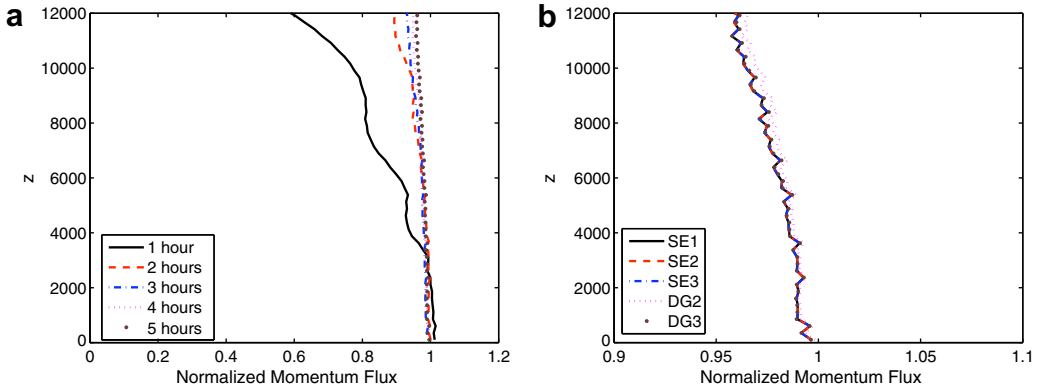

Fig. 13. Case 7: Linear Nonhydrostatic Mountain. Normalized momentum flux for 360 m (in x) and 300 m (in z) resolution and 10th order polynomials for (a) DG3 at times 1, 2, 3, 4, and 5 h, and (b) for all five models at 5 h.

Table 8
Case 7: Linear nonhydrostatic mountain

Variable	SE1	SE2	SE3	DG2	DG3
π	1.69×10^{-8}	1.62×10^{-8}	1.62×10^{-8}	1.65×10^{-8}	1.61×10^{-8}
u	4.85×10^{-4}	4.84×10^{-4}	4.84×10^{-4}	4.79×10^{-4}	4.80×10^{-4}
w	9.39×10^{-5}	9.39×10^{-5}	9.39×10^{-5}	6.57×10^{-5}	8.94×10^{-5}
θ	1.69×10^{-4}	1.69×10^{-4}	1.69×10^{-4}	1.67×10^{-4}	1.68×10^{-4}

Root-mean-square errors for all four variables for 360 m (in x) and 300 m (in z) resolution and 10th order polynomials after 10 h for all five models.

models. The results for this test can be summarized as follows: all models performed quite similarly, however, sets 2 and 3 are preferred over set 1 and DG is preferred over SE.

6.8. Conservation and efficiency

A few words regarding the conservation properties and efficiency of the models are in order. We have discussed the three equation sets and have mentioned that only sets 2 and 3 are formally conservative. However,

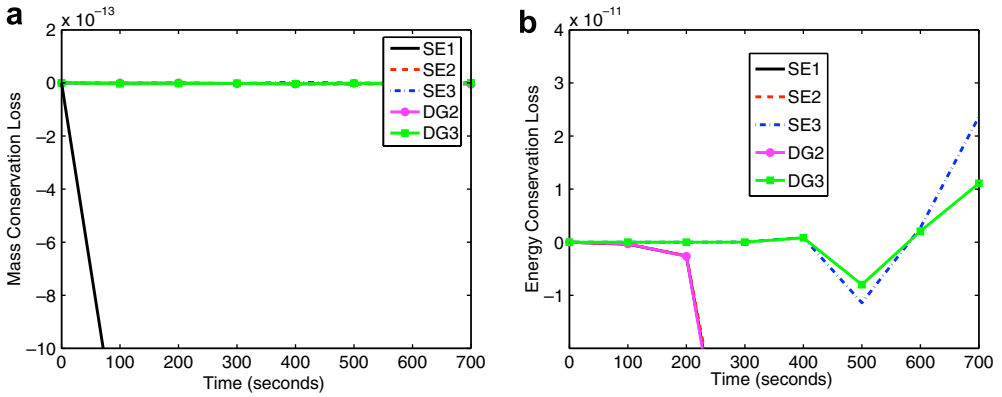

Fig. 14. Conservation of (a) mass and (b) energy for all five models using the *strong* form. The results shown are for the rising thermal bubble using a 20 m resolution with 10th order polynomials.

the question that needs to be addressed is what exactly are these equations conserving. For equation set 3 the answer is obvious since the governing equations consist of three conservation laws for mass, momentum, and total energy. For set 2, the conserved quantities are mass, momentum, and density potential temperature. For set 1, none of the variables should be conserved. Fig. 14 shows the loss of mass (left panel) and energy (right panel) conservation for all five models using the strong form of the equations (Eqs. (23) and (32)). As expected, Fig. 14a shows that the only model that does not conserve mass is set 1 (SE1); it should be understood that this is not a problem with the numerical method but rather with the governing equation – this form cannot formally conserve any quantity. Fig. 14b shows that the only models which conserve energy are SE3 and DG3, that is, those that use set 3. On the other hand, SE1, SE2, and DG2 do not conserve energy. We know already that set 1 will not conserve any quantity, however, set 2 does not conserve total energy but it does in fact conserve density potential temperature (not shown). Potential temperature is directly related to entropy and therefore it makes more sense to conserve energy than to impose the model to be isentropic. Perhaps once physical parameterization (in the form of source functions in momentum and energy) is added to the equations to represent sub-grid scale processes, the debate whether conserving total energy or entropy becomes moot. We plan to revisit this issue in future work where we shall experiment with simple physical parameterizations.

Note that while the energy conservation given in Fig. 14b is quite good, it is not conservative up to machine precision. This is due to the inexact integration we use for both the SE and DG methods. However, if the weak form of the equations are used (Eqs. (25) and (31)), then SE3 and DG3 are conservative up to machine precision (10^{-16}) which we show in Fig. 15b.

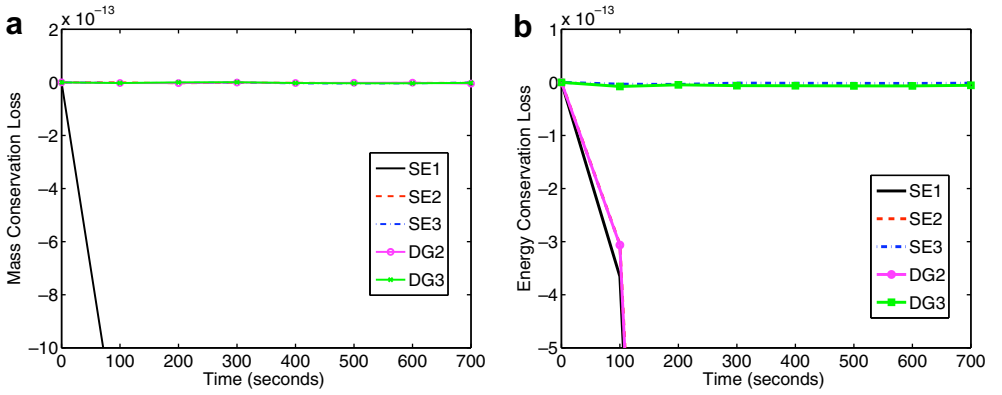

Fig. 15. Conservation of (a) mass and (b) energy for all five models using the *weak* form. The results shown are for the rising thermal bubble using a 20 m resolution with 10th order polynomials.

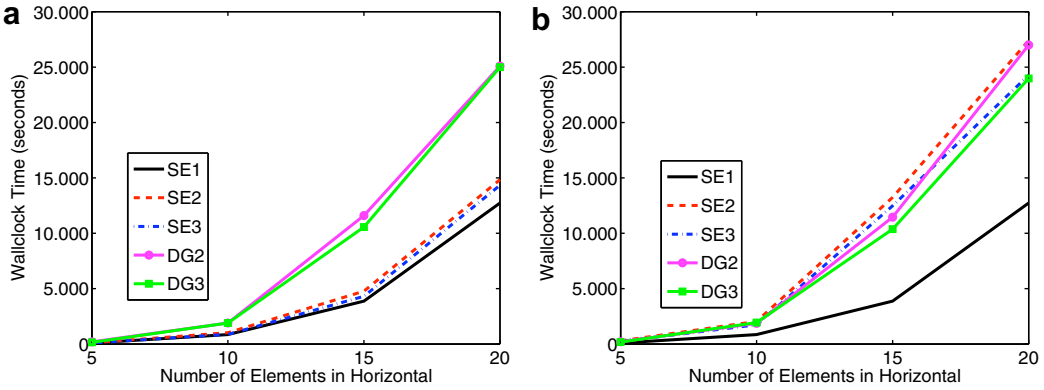

Fig. 16. Efficiency of the (a) strong and (b) weak forms of the equations for all five models. The results shown are for the rising thermal bubble using various number of elements in the horizontal (with equal number in the vertical) using 10th order polynomials with an integration time of 700 s.

While we have not devoted a lengthy discussion to the efficiency comparisons of the five models, we should mention that the DG models are, in general, more computationally expensive than the SE models. The reason for the heavier costs incurred by DG methods is due to the fact that the DG method requires the computation of area integrals typical of SE methods as well as boundary integrals typical of FV methods. The cost of area integrals is $O(N_e N^3)$ where N_e are the number of elements and N is the order of the polynomial. The cost of boundary integrals is $O(N_s N)$ where N_s is the number of sides/edges. For viscous problems, additional floating point operations of $O(N_e N^3)$ are required by the *local discontinuous Galerkin* (LDG) method. To give the reader a sense of these costs, in Fig. 16 we plot the wallclock time required by all five models to integrate 700 s for the rising thermal bubble for various resolutions. Recall that the rising thermal bubble (case 2) is solved on a square domain with equal resolution in the horizontal (x) and vertical (z) directions. In Fig. 16a we plot the wallclock time for all five models using the strong form of the equations which are not guaranteed to conserve exactly even for sets 2 and 3. We should point out, however, that this is the worst case scenario for the DG method – meaning that for these timings, we have used the maximum time-steps allowed by the SE models which are 50% larger than those allowed by the DG models.

If we impose conservation, then the equations have to be solved in weak form and the maximum allowable time-step for the SE method is less than or equal to that for the DG method; this slightly larger time-step allows the DG method (although it requires more floating point operations) to compete with the SE method. Comparing the weak form solutions, Fig. 16b shows that the DG models are now as efficient as the SE models; note that we have also plotted the SE1 solution although this form is not conservative even in the weak form. Another observation regarding the efficiency of the three equation sets is that set 3 is more efficient to compute than set 2, and set 1 is more efficient than sets 2 and 3. The reason has to do with the cost of computing the pressure. For set 1, the pressure (Exner in this case) is in fact a prognostic variable whereas for sets 2 and 3 it is diagnostic and hence has to be computed from the prognostic variables. For set 2, the pressure is a function of the prognostic variables raised to an exponent (see Eq. (5)) whereas for set 3, the pressure is a linear function of the prognostic variables (see Eq. (8)) and therefore cheaper to compute. This brief discussion on the cost of the SE and DG methods is completely independent from the time-integrators used. In this work we only discuss explicit methods but in a separate paper we present semi-implicit results [41].

7. Conclusions

In this paper we studied three forms of the Euler equations for possible use in next-generation nonhydrostatic models. Set 1 is not in conservation form; set 2 can be written in conservation form only for inviscid flow; while set 3 can be written in conservation form for either inviscid or viscous flow applications and is in fact the compressible Navier–Stokes (NS) equations. We compared the results of the three equation sets

using two numerical methods: the spectral element (SE) and discontinuous Galerkin (DG) methods; both are local high-order methods but the DG method is a fully conservative method (both global and local) while the SE method is only globally conservative. We tested the five models using seven test cases: three of which involved mountain waves. The five models gave similar results and compare well with models found in the literature. Equation set 1, although not in conservation form, performed better than expected although it tended to yield slightly different results than sets 2 and 3. The differences between the five models were quite small but the main result found is that the differences in the simulation were most often attributed to the equation set used; the numerical method also played a role in the performance of the models. Set 3 (fully compressible NS equations) yielded solutions that were less dissipative (for the density current). The comparison of the SE and DG methods showed that both methods yield similar solutions for the types of problems studied; however, for the bubble and mountain tests, the DG method performed better. It is expected that for more stringent tests (i.e. those having very steep gradients such as those produced by the sub-grid scale parameterization) the DG method will prevail. In future work we will explore high-order non-reflecting boundary conditions and add sub-grid scale parameterization to study the sensitivity of these methods to the sharp local gradients it produces. Although it is too early to conclude which equation set and method will work best with the parameterization, we expect the DG method to handle the sub-grid scale processes better due to its ability to better handle discontinuities (as in the two bubble problems). The exact conservation properties of set 3 in its weak form motivates us to pursue this equation set in our future studies.

Acknowledgments

The first author (FXG) gratefully acknowledges the support of the Office of Naval Research through program element PE-0602435N. Both authors thank the Office of Naval Research which provided partial support for the second author through the Visiting Scientist Program.

References

[1] N. Ahmad, J. Lindeman, Euler solutions using flux-based wave decomposition, International Journal for Numerical Methods in Fluids 54 (2007) 41–72.
[2] V. Aizinger, C. Dawson, A discontinuous Galerkin method for two-dimensional flow and transport in shallow water, Advances in Water Resources 25 (2002) 67–84.
[3] F. Bassi, S. Rebay, A high-order accurate discontinuous finite element method for the numerical solution of the compressible Navier–Stokes equations, Journal of Computational Physics 131 (1997) 267–279.
[4] R. Benoit, M. Desgagné, P. Pellerin, S. Pellerin, Y. Chartier, S. Desjardins, The Canadian MC2: A semi-Lagrangian, semi-implicit wideband atmospheric model suited for finescale process studies and simulation, Monthly Weather Review 125 (1997) 2382–2415.
[5] L. Bonaventura, A semi-implicit, semi-Lagrangian scheme using the height coordinate for a nonhydrostatic and fully elastic model of atmospheric flows, Journal of Computational Physics 158 (2000) 186–213.
[6] J. Boyd, The erfc-log filter and the asymptotics of the Euler and Vandeven sequence accelerations, in: A.V. Ilin, L.R. Scott (Eds.), Proceedings of the Third International Conference on Spectral and High Order Methods, Houston Journal of Mathematics, Houston, Texas, 1996, pp. 267–276.
[7] R.L. Carpenter, K.K. Droegemeier, P.R. Woodward, C.E. Hane, Application of the piecewise parabolic method (PPM) to meteorological modeling, Monthly Weather Review 118 (1990) 586–612.
[8] B. Cockburn, C.-W. Shu, The local discontinuous Galerkin method for time-dependent convection–diffusion systems, SIAM Journal on Numerical Analysis 35 (1998) 2440–2463.
[9] B. Cockburn, C.-W. Shu, Runge–Kutta discontinuous Galerkin methods for convection-dominated problems, Journal of Scientific Computing 16 (2001) 173–261.
[10] F. Dupont, C.A. Lin, The adaptive spectral element method and comparisons with more traditional formulations for ocean modeling, Journal of Atmospheric and Oceanic Technology 21 (2004) 135–147.
[11] D.R. Durran, J.B. Klemp, A compressible model for the simulation of moist mountain waves, Monthly Weather Review 111 (1983) 2341–2361.
[12] C. Eskilsson, S.J. Sherwin, A triangular spectral/hp discontinuous Galerkin method for modelling 2D shallow water equations, International Journal for Numerical Methods in Fluids 45 (2004) 605–623.
[13] A. Fournier, H.P. Bunge, R. Hollerbach, J.P. Vilotte, Application of the spectral element method to the axisymmetric Navier–Stokes equations, Geophysical Journal International 156 (2004) 682–700.
[14] A. Fournier, M.A. Taylor, J.J. Tribbia, The spectral element atmosphere model (SEAM): high-resolution parallel computation and localized resolution of regional dynamics, Monthly Weather Review 132 (2004) 726–748.

[15] O. Friedrich, Weighted essentially non-oscillatory schemes for the interpolation of mean values on unstructured grids, Journal of Computational Physics 144 (1998) 194–212.
[16] T. Gal-Chen, C.J. Somerville, On the use of a coordinate transformation for the solution of the Navier–Stokes equations, Journal of Computational Physics 17 (1975) 209–228.
[17] A. Gassmann, An improved two-time-level split-explicit integration scheme for non-hydrostatic compressible models, Meteorology and Atmospheric Physics 88 (2005) 23–38.
[18] F.X. Giraldo, A space marching adaptive remeshing technique applied to the 3D Euler equations for supersonic flow, PhD thesis, University of Virginia, 1995.
[19] F.X. Giraldo, Lagrange–Galerkin spectral element methods on unstructured quadrilateral grids, Journal of Computational Physics 147 (1998) 114–146.
[20] F.X. Giraldo, J.S. Hesthaven, T. Warburton, Nodal high-order discontinuous Galerkin methods for the spherical shallow water equations, Journal of Computational Physics 181 (2002) 499–525.
[21] F.X. Giraldo, T.E. Rosmond, A scalable spectral element Eulerian atmospheric model (SEE-AM) for NWP: dynamical core tests, Monthly Weather Review 132 (2004) 133–153.
[22] F.X. Giraldo, T. Warburton, A nodal triangle-based spectral element method for the shallow water equations on the sphere, Journal of Computational Physics (2005).
[23] F.X. Giraldo, High-order triangle-based discontinuous Galerkin methods for hyperbolic equations on a rotating sphere, Journal of Computational Physics 214 (2006) 447–465.
[24] F.X. Giraldo, T. Warburton, A high-order triangular discontinuous Galerkin coastal ocean model: barotropic formulation, International Journal for Numerical Methods in Fluids (2008), in press, doi:10.1002/fld.1562.
[25] G. Grell, J. Dudhia, D. Stauffer, A description of the fifth-generation Penn State/NCAR Mesoscale Model (MM5), NCAR Technical Note NCART/TN-398+STR, 1995.
[26] R.M. Hodur, The Naval Research Laboratory's coupled ocean/atmosphere mesoscale prediction system (COAMPS), Monthly Weather Review 125 (1997) 1414–1430.
[27] C.Q. Hu, C.W. Shu, Weighted essentially non-oscillatory schemes on triangular meshes, Journal of Computational Physics 150 (1999) 97–127.
[28] M. Iskandarani, D.B. Haidvogel, J.C. Levin, A three-dimensional spectral element model for the solution of the hydrostatic primitive equations, Journal of Computational Physics 186 (2003) 397–425.
[29] Z. Janjić, A nonhydrostatic model based on a new approach, Meteorology and Atmospheric Physics 82 (2003) 271–285.
[30] J.B. Klemp, D.K. Lilly, Numerical simulation of hydrostatic mountain waves, Journal of the Atmospheric Sciences 35 (1978) 78–107.
[31] J.B. Klemp, R.B. Wilhelmson, The simulation of three-dimensional convective storm dynamics, Journal of the Atmospheric Sciences 35 (1978) 1070–1096.
[32] J.B. Klemp, D.R. Durran, An upper boundary condition permitting internal gravity wave radiation in numerical mesoscale models, Monthly Weather Review 111 (1983) 430–444.
[33] D. Komatitsch, J. Tromp, Introduction to the spectral element method for three-dimensional seismic wave propagation, Geophysics Journal International 139 (1999) 806–822.
[34] E.J. Kubatko, J.J. Westerink, C. Dawson, hp discontinuous Galerkin methods for advection dominated problems in shallow water flow, Computer Methods in Applied Mechanics and Engineering 196 (2006) 437–451.
[35] H. Li, R.X. Liu, The discontinuous Galerkin finite element method for the 2d shallow water equations, Mathematics and Computers in Simulation 56 (2001) 171–184.
[36] Y. Liu, Marcel Vinokur, Z.J. Wang, Spectral difference method for unstructured grids I: basic formulation, Journal of Computational Physics 216 (2006) 780–801.
[37] R.D. Nair, S.J. Thomas, R.D. Loft, A discontinuous Galerkin global shallow water model, Monthly Weather Review 133 (2005) 876–888.
[38] T.M. Ozgokmen, P.F. Fischer, J.Q. Duan, T. Iliescu, Three-dimensional turbulent bottom density currents from a high-order nonhydrostatic spectral element model, Journal of Physical Oceanography 34 (2004) 2006–2026.
[39] J.P. Pinty, R. Benoit, E. Richard, R. Laprise, Simple tests of a semi-implicit semi-Lagrangian model on 2D mountain wave problems, Monthly Weather Review 123 (1995) 3042–3058.
[40] J.F. Remacle, S.S. Frazão, X.G. Li, M.S. Shephard, An adaptive discretization of shallow-water equations based on discontinuous Galerkin methods, International Journal for Numerical Methods in Fluids 52 (2006) 903–923.
[41] M. Restelli, F.X. Giraldo, A conservative semi-implicit discontinuous Galerkin method for the Navier–Stokes equations in nonhydrostatic mesoscale atmospheric modeling, SIAM Journal on Scientific Computing submitted (2007).
[42] A. Robert, Bubble convection experiments with a semi-implicit formulation of the Euler equations, Journal of the Atmospheric Sciences 50 (1993) 1865–1873.
[43] C. Schär, D. Leuenberger, O. Fuhrer, D. Lüthic, C. Girard, A new terrain-following vertical coordinate formulation for atmospheric prediction models, Monthly Weather Review 130 (2002) 2459–2480.
[44] D. Schwanenberg, J. Köngeter, A discontinuous Galerkin method for the shallow water equations with source terms, in: B. Cockburn, G.E. Karniadakis, C.-W. Shu (Eds.), Discontinuous Galerkin Methods, Springer, Heidelberg, 2000, pp. 289–309.
[45] C.W. Shu, High-order finite difference and finite volume WENO schemes and discontinuous Galerkin methods for CFD, International Journal of Computational Fluid Dynamics 17 (2003) 107–118.
[46] W.C. Skamarock, J.B. Klemp, Efficiency and accuracy of the Klemp–Wilhelmson time-splitting technique, Monthly Weather Review 122 (1994) 2623–2630.

[47] W.C. Skamarock, J.D. Doyle, P. Clark, N. Wood, A standard test set for nonhydrostatic dynamical cores of NWP models, AMS NWP-WAF Conference Poster P2.17, 2004, Additionally, see <www.mmm.ucar.edu/projects/srnwp_tests/>.
[48] W.C. Skamarock, J.B. Klemp, J. Dudhia, D.O. Gill, D.M. Baker, W. Wang, J.G. Powers, A description of the Advanced Research WRF Version 2, NCAR Technical Note NCART/TN-468+STR, 2007.
[49] R.B. Smith, The influence of mountains on the atmosphere, Advances in Geophysics 21 (1979) 87.
[50] R.J. Spiteri, S.J. Ruuth, A new class of optimal high-order strong-stability-preserving time discretization methods, SIAM Journal of Numerical Analysis 40 (2002) 469–491.
[51] J.M. Straka, R.B. Wilhelmson, L.J. Wicker, J.R. Anderson, K.K. Droegemeier, Numerical solutions of a non-linear density current: a benchmark solution and comparisons, International Journal for Numerical Methods in Fluids 17 (1993) 1–22.
[52] M.A. Taylor, A. Fournier, Local mass and energy conservation in spectral-element discretizations of the sphere (& torus), workshop "Solution of Partial Differential Equations on the Sphere", Exeter, 2007.
[53] S.J. Thomas, R.D. Loft, J.M. Dennis, Parallel implementation issues: global versus local methods, Computing in Science and Engineering 4 (2002) 26–31.
[54] E. Toro, Riemann Solvers and Numerical Methods for Fluid Dynamics, Springer, New York, 2001, p. 449.
[55] E. Toro, Shock-Capturing Methods for Free-surface Shallow Flows, Wiley, New York, 2001, p. 245.
[56] Z.J. Wang, L. Zhang, Y. Liu, Spectral (finite) volume method for conservation laws on unstructured grids IV: extension to two-dimensional systems, Journal of Computational Physics 194 (2004) 716–741.
[57] L. Wicker, W.C. Skamarock, A time-splitting scheme for the elastic equations incorporating second-order Runge–Kutta time differencing, Monthly Weather Review 126 (1998) 1992–1999.
[58] L. Wicker, W.C. Skamarock, Time-splitting methods for elastic models using forward time schemes, Monthly Weather Review 130 (2002) 2088–2097.
[59] D. Xiu, G.E. Karniadakis, A semi-Lagrangian high-order method for the Navier–Stokes equations, Journal of Computational Physics 172 (2001) 658–684.
[60] M. Xue, K.K. Droegemeier, V. Wong, The advanced regional prediction system (ARPS) – a multi-scale nonhydrostatic atmospheric simulation and prediction model. Part I: Model dynamics and verification, Meteorology and Atmospheric Physics 75 (2000) 161–193.